ADVANCED MATERIALS
www.advmat.de

Control of Two Solid Electrolyte Interphases at the Negative Electrode of an Anode-Free All Solid-State Battery based on Argyrodite Electrolyte

Yixian Wang, Vikalp Raj,* Kaustubh G. Naik, Bairav S. Vishnugopi, Jaeyoung Cho, Mai Nguyen, Elizabeth A. Recker, Yufeng Su, Hugo Celio, Andrei Dolocan, Zachariah A. Page, John Watt, Graeme Henkelman, Qingsong Howard Tu, Partha P. Mukherjee, and David Mitlin**

Anode-free all solid-state batteries (AF-ASSBs) employ "empty" current collector with three active interfaces that determine electrochemical stability; lithium metal – Solid electrolyte (SE) interphase (SEI-1), lithium – current collector interface, and collector – SE interphase (SEI-2). Argyrodite Li_6PS_5Cl (LPSCl) solid electrolyte (SE) displays SEI-2 containing copper sulfides, formed even at open circuit. Bilayer of 140 nm magnesium/30 nm tungsten (Mg/W-Cu) controls the three interfaces and allows for state-of-the-art electrochemical performance in half-cells and fullcells. AF-ASSB with NMC811 cathode achieves 150 cycles with Coulombic efficiency (CE) above 99.8%. With high mass-loading cathode (8.6 mAh cm^{-2}), AF-ASSB retains 86.5% capacity after 45 cycles at 0.2C. During electrodeposition of Li, gradient Li-Mg solid solution is formed, which reverses upon electrodissolution. This promotes conformal wetting/dewetting by Li and stabilizes SEI-1 by lowering thermodynamic driving force for SE reduction. Inert refractory W underlayer is required to prevent ongoing formation of SEI-2 that also drives electrochemical degradation. Inert Mo and Nb layers likewise protect Cu from corroding, while Li-alloying layers (Mg, Sn) are less effective due to ongoing volume changes and associated pulverization. Mechanistic explanation for observed Li segregation within alloying Li_xMg layer is provided through mesoscale modelling, considering opposing roles of diffusivity differences and interfacial stresses.

1. Introduction

All-solid-state batteries (ASSBs) have the potential to address the increasing safety and energy demands for next-generation electrochemical energy storage systems, including for electric vehicles (EVs).[1–8] ASSBs hold promise for achieving a specific energy of 500 Wh kg^{-1} at the cell-level, particularly when coupled with high-voltage cathode materials such as $LiNi_{0.8}Mn_{0.1}Co_{0.1}O_2$ (NMC811) and $LiNi_{0.5}Mn_{1.5}O_4$ (LNMO).[9–15] The incorporation of inorganic solid electrolytes (SEs) further enhances the appeal of ASSBs as these materials are either nonflammable or exhibit exceptionally high ignition temperatures, thereby offering superior safety features compared to their counterparts utilizing liquid electrolytes.[16–18] Sulfide-based SEs stand out for their high Li-ionic conductivities and advantageous physical "softness" that enables enhanced formability. Argyrodite-type Li_6PS_5Cl (LPSCl) sulfide SE has demonstrated a combined advantage

Y. Wang, V. Raj, Y. Su, H. Celio, A. Dolocan, D. Mitlin
Materials Science and Engineering Program
Walker Department of Mechanical Engineering and Texas Materials Institute
The University of Texas at Austin
Austin, TX 78712, USA
E-mail: yixwang@utexas.edu; vikalp.raj@austin.utexas.edu; david.mitlin2@utexas.edu

K. G. Naik, B. S. Vishnugopi, P. P. Mukherjee
School of Mechanical Engineering
Purdue University
West Lafayette, IN 47907, USA

J. Cho, M. Nguyen, E. A. Recker, Z. A. Page, G. Henkelman
Department of Chemistry
The University of Texas at Austin
Austin, TX 78712, USA

E. A. Recker
McKetta Department of Chemical Engineering
The University of Texas at Austin
Austin, TX 78712, USA

J. Watt
Center for Integrated Nanotechnologies
Los Alamos National Laboratory
Los Alamos, NM 87545, USA

Q. H. Tu
Department of Mechanical Engineering
Rochester Institute of Technology
Rochester, NY 14623, USA

The ORCID identification number(s) for the author(s) of this article can be found under https://doi.org/10.1002/adma.202410948

DOI: 10.1002/adma.202410948

of an acceptable ionic conductivity (≈1 mS cm^{-2}) with some degree of self-passivation at both the anode-SE and cathode-SE interphases,[19–23] the later not typically possible with other sulfide electrolytes.

Yet despite many advancements the implementation of any sulfide SE, including of argyrodite, in ASSBs presents several serious challenges. One critical issue is the inherent reactivity between sulfides and both electrodes, resulting in electrolyte/electrode decomposition that increases cell impedance and fosters the formation of a mixed conducting interphase (MCI).[24–27] The interface between the metal anode and the SE should ideally be thermodynamically stable or passivated to be kinetically stable. However, sulfide SEs are not thermodynamically stable at 0 V versus Li/Li^+, leading to the formation of either MCI or a (partially) kinetically stabilized solid electrolyte interphase (SEI).[28–31] It has been recently demonstrated that even LPSCl, which was assumed to be kinetically self-passivated, continues to decompose through reaction with Li during electrochemical cycling.[32–34] Li et al. conducted a study on the corrosion behavior of copper current collectors in relation to moisture levels. They discovered that even minimal water presence causes Cu to react with hydrogen sulfide (H_2S), produced by the hydrolysis of sulfide SE, resulting in the formation of a copper sulfide (Cu_2S) layer.[35] With LPSCl, Li-SE reaction induced voids in the metal have been reported.[32] Kirkendall-type porosity in the lithium foil may be caused by the significant site-to-site variations in the thickness of the formed SEI during cycling or storage, as documented by cryogenic electron microscopy and Raman mapping. At reacted region there was also voiding in the decomposed LPSCl due to the reaction products being denser than the parent materials. Such reactivity will also lead to the lithium metal and the SE pulling away from each other. Lithium metal dendrite growth has also been reported at the Li-SE interphase, with a recent study employing site-specific electron microscopy to image a branched intergranular sheet-like dendrite that has shorted an LPSCl symmetric cell.[36–39] For ASSBs utilizing sulfides, cell failure may occur gradually through impedance rise or suddenly and catastrophically through short-circuiting.

A "conventional" ASSB employed a metallurgically rolled Li foil as the anode.[40–42] However for a relatively thick lithium foil the capacity of the two electrodes is imbalanced and the cell energy is not optimized. For example, the capacity of a 100 µm Li foil is 20 mAh cm^{-2}, versus a commercially relevant cathode that is at 4 mAh cm^{-2}. To achieve ASSBs with the targeted 400 or 500 Wh kg^{-1} energy, it is necessary to limit the amount of Li utilized.[43–45] This also reduces cell cost and increases safety, since oxidation of Li metal is a highly exothermic process. An anode-free all-solid-state battery (AF-ASSB) configuration emerges as the targeted architecture, where all the active Li is stored in the cathode, the same way it is in conventional LIBs.[46–49] AF-ASSBs may offer over 50% higher energy by volume as compared to conventional cells that employ rolled sheets of Li metal. Pioneering studies on AF-ASSBs were focused on thin-film solid-state batteries using Li phosphorus oxynitride (LiPON) electrolyte.[50] LiPON electrolyte is kinetically stable with Li and is straightforward to deposit as a thin film using magnetron sputtering.[51,52] However its relatively low ionic conductivity (≈10^{-6} S cm^{-1}) limits its applications. Another seminal study demonstrated the feasibility of a non-reactive garnet solid electrolyte $Li_7La_3Zr_2O_{12}$ (LLZO) for AF-ASSBs.[53] Recently there have been a number of important advances in the interfacial science and in architecture design of sulfide-based ASSBs.[54–61] Despite these findings, achieving long-term electrochemical stability in sulfide-based ASSBs is not feasible yet.

As will be demonstrated, with AF-ASSBs the critical unexplored challenge is that there are two solid electrolyte interphase layers (SEI-1 and SEI-2) at the negative electrode. Electrochemical stability in an AF-ASSB based on argyrodite SE requires microstructural control of three interfaces; (i) the lithium metal – SE interface has to remain uniform and passivated, forming the first SEI layer (SEI-1), (ii) the Li-Cu current collector interface has to remain wetted, (iii) and the Cu-SE interface has to remain minimally corroded, forming effectively what is a second SEI layer (SEI-2). This work elucidates the necessary role of the underlying refractory W layer in protecting the current collector from parasitic reactions with the sulfur species in the SE so as to control SEI-2. To date, this second SEI layer has received minimal scientific attention. With bilayer Mg/W-Cu state-of-the-art electrochemical performance is obtained using an AF-ASSB with commercially relevant cathode mass loading.

This study provides a comprehensive explanation of the complex functionality of the Mg layer in promoting uniform Li metal electrodeposition/dissolution and consequently stabilizing the Li-SE interphase. The electrodeposition stress promotes Li-deficiency in the Li-Mg alloy next to the electrolyte, which is the opposite of what is expected based on just diffusivity differences. The Mg-rich portion of the Li-Mg layer is thermodynamically less reactive with the electrolyte. While Mg is a known current collector coating layer that enhances overall electrochemical stability of solid and liquid electrolyte metal batteries, its functionality to-date has not been well understood. Analytical techniques including cryogenic focused ion beam (cryo-FIB) microscopy are combined with atomic and mesoscale simulations to provide a comprehensive phenomenological description of the underlying phase transformations. Having identified the mechanisms by which SEI-1 and SEI-2 may be controlled, this work may serve as an important steppingstone for advancing AF-ASSB microstructural design.

2. Results and Discussion

Bilayer magnesium tungsten coated copper current collector (Mg/W-Cu) was fabricated by physical vapor deposition (PVD, magnetron sputtering). A schematic illustration of the process being shown in **Figure 1a** with details being provided in the Supporting Information. A battery-grade copper foil (5 cm × 5 cm, 9 µm thickness) served as the substrate, which was mounted onto a holder and subsequently transferred into the sputtering chamber and evacuated to a base pressure below 10^{-8} torr. Pure Mg and W metal disks with a diameter of 2 inches and a thickness of 0.25 inch were used as the targets. A layer of W followed by a layer of Mg was successively deposited onto the Cu collector foil with the sputter rate calibrated using a quartz crystal monitor. The W layer interfaced the Cu, while the Mg layer would interface with the SE when joined in a cell. For comparison, magnesium-coated copper foil (Mg-Cu) and tungsten-coated copper foil (W-Cu) were prepared using a similar approach.

Figures S1 and S2 (Supporting Information), and Figure 1b present the top down scanning electron microscopy (SEM) and

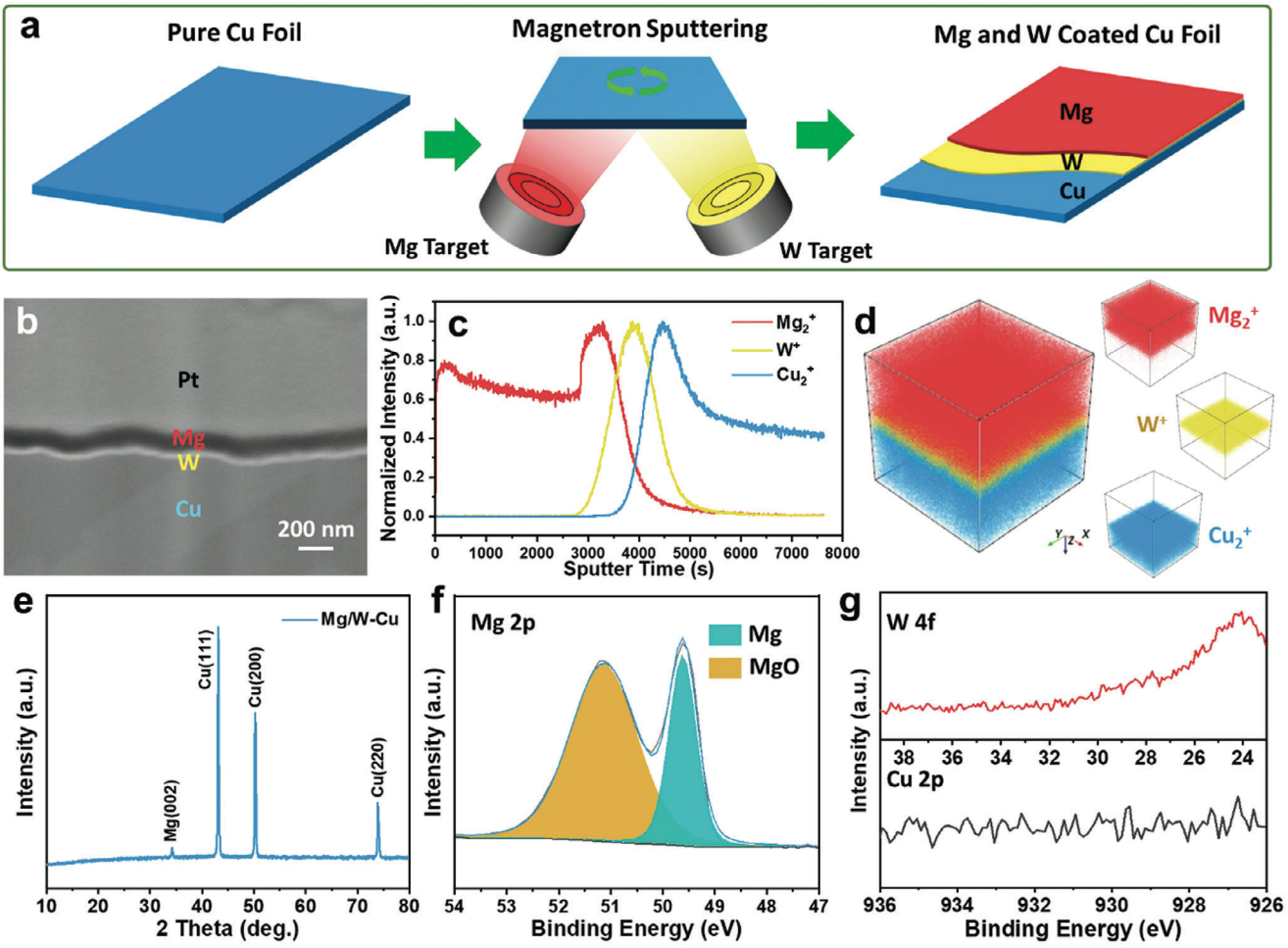

Figure 1. a) Schematic illustration for the fabrication process of Mg (top) and W (bottom) coated Cu foil, termed Mg/W-Cu. b) Cross-sectional FIB-SEM image, c,d) TOF-SIMS depth profiles and 3D rendering of Mg_2^+, W^+, and Cu_2^+ fragments, e) XRD profile, and f,g) High-resolution Mg 2p, W 4f, and Cu 2p spectra of Mg/W-Cu.

cross sectional focused ion beam (FIB) SEM analysis of Mg/W–Cu, Mg–Cu, and W–Cu current collectors. Figure 1c,d showcase the topological information of the Mg/W–Cu sample using time-of-flight secondary ion mass spectrometry (TOF-SIMS). Figures 1e and S3 (Supporting Information) compare the X-ray diffraction (XRD) profiles of Mg/W-Cu, Mg-Cu, and W-Cu. Figure 1f,g shows the high-resolution X-ray photoelectron spectroscopy (XPS) spectra of Mg 2p, W 4f, and Cu 2p for Mg/W-Cu. Figure 1b, Figure S2c,f (Supporting Information) provides the cross-sectional images of Mg/W-Cu, Mg-Cu, and W-Cu, respectively. ≈1 µm thickness platinum (Pt) layer was deposited using the gas injection system (GIS) and cured with a Ga-ion beam prior to ion milling to protect the surface from beam damage. The measured thickness is ≈140 nm for the sputtered Mg layer and ≈30 nm for the sputtered W layer in the Mg/W-Cu sample. The images were captured using an ion conversion and electron (ICE) detector in secondary electron (SE) mode, where heavy elements typically exhibit a brighter contrast compared to light elements due to the emission of more backscattered electrons. Consequently, the Mg layer appears darker than the Cu substrate while the W layer appears brighter. The thicknesses of Mg layer and W layer in the Mg-Cu and W-Cu specimens are measured to be ≈160 and ≈260 nm, respectively.

To further elucidate the bilayer structure of the Mg/W-Cu sample, Figure 1c shows the TOF-SIMS depth profiles of three representative species: Mg_2^+, W^+, and Cu_2^+. During the initial 2850 s of sputtering, only Mg_2^+ signal can be detected. Subsequently, the W^+ signal emerges and followed by the appearance of the Cu_2^+ signal after 3500 s. The sudden increase of Mg_2^+ intensity at the Mg/W interface is likely associated with the so-called matrix effect that indicates a change in ionization probability of the detected species due to the electron work function difference at the interface: 3.7 eV for Mg versus 4.6 eV for W.[62] Figure 1d shows a 3D rendering of the selected species representing Mg, W, and Cu, indicating the uniform deposition of Mg and W to form the bi-layer structure. It should be noted that per the equilibrium phase diagram the Mg and the W possess minimal miscibility. Sputtering Mg onto the W layer could introduce some non-equilibrium mixing at the atomic scale. However it should be low since W (183.84 u) is much heavier than the Mg (24.305 u) and is not expected to be resputtered during the Mg deposition.

Figures S1, S2a,b, and S2d,e (Supporting Information) provide the top-down SEM images of Mg/W-Cu, Mg-Cu, and W-Cu, respectively. The surfaces of Mg/W-Cu and Mg-Cu display a morphology dictated by the hexagonal shaped Mg crystals. Both the Mg/W-Cu and Mg-Cu surfaces exhibit homogeneously distributed hexagonal Mg grains with lateral dimensions ranging from 200 to 300 nm. By contrast, the surface of the W-Cu sample is dense, relatively planar, and without discernible crystallites. This is expected since the lower melting Mg will diffuse faster and therefore undergo greater degree of grain growth during sputter deposition versus refractory W. XRD measurements were performed to analyze the crystal structure of the coating layers, and the results are presented in Figures 1e and S3 in the Supporting Information. All samples exhibit diffraction peaks at 43.3°, 50.43°, and 74.13°, corresponding to the (111), (200), (220) reflections in *fcc* Cu (a = 0.3615 nm, #04-0836) with Fm-3m space group. An additional peak at 34.4° is observed for the Mg-Cu sample, which is attributed to the (002) reflection in *hcp* Mg (a = 3.2096 nm, c = 5.2112 nm, #35-0821) with P63/mmc space group. This agrees with the hexagonal grain morphology of the Mg films, with (001) basal plane of the crystallites being parallel to the substrate surface and [100] and [010] being the fast growth directions. Such film growth kinetics are well-known for hexagonal metals such as Mg and Zn. For the W-Cu sample, three additional peaks occur at 40.26°, 58.27°, and 73.2°, which are ascribed to the (110), (200), and (211) planes of *bcc* W (a = 3.1648 nm, #04-0806) with Im-3m space group. The Mg/W-Cu sample only displays the Bragg peak at 34.4°, corresponding to (002) plane of Mg. The absence of W diffraction peaks is due to the 30 nm thickness, where the scattered intensity falls below the detection limit of the benchtop XRD instrument. Additionally, the mean grain size of the 30 nm film is expected to be finer than that of the 260 nm W-Cu film, causing more peak broadening and making it more difficult to detect above the background.

XPS analysis was conducted to investigate the surface chemistry of Mg-W/Cu, Mg-Cu, and W-Cu. Figure 1f shows the high-resolution Mg 2p spectrum, revealing two distinct peaks. The peak at 49.6 eV is attributed to Mg metal while the peak at 51.5 eV is ascribed to the native MgO layer spontaneously formed on the surface. Magnesium oxide is thermodynamically stable with a standard enthalpy of formation of –601.6 kJ mol^{-1}, which is on the same order as for Li_2O –598.7 kJ mol^{-1}. At ambient conditions surface growth of MgO effectively ceases once 2–3 nm thickness is reached. However it appears that additional oxidation may have occurred during the sputtering process due to residual water vapor and oxygen in the system, giving a stronger peak intensity that would be expected from 2 to 3 nm. Figure 1g presents the high-resolution W 4f and Cu 2p spectra of the Mg-W/Cu sample. No characteristic peak for either element is observed, indicating that the Mg layer fully covers the surface. This observation aligns with the TOF-SIMS analysis results. Surface XPS analysis for Mg-Cu is provided in Figure S4a,b in the Supporting Information. Both Mg and MgO are detected, while representative Cu signals are absent. The results for W-Cu are illustrated in Figure S4c,d in the Supporting Information. The W 4f spectrum of W-Cu exhibits three doublets of peaks, corresponding to tungsten metal (31.3 and 33.5 eV for $4f_{7/2}$ and $4f_{5/2}$), tungsten suboxide (WO_x, 32.0 and 34.2 eV for $4f_{7/2}$ and $4f_{5/2}$), and tungsten oxide (WO_3, 35.5 and 37.7 eV for $4f_{7/2}$ and $4f_{5/2}$), respectively. The Cu signal is absent, indicating coverage of the surface by the W layer. In sum, the XPS findings confirm that the bilayer and single layer films are conformal to the current collector.

The mechanical properties of the Cu foils before and after sputtering were measured using a nanoindentation system equipped with a Berkovich diamond tip. The load function involved loading the sample to a maximum displacement of 500 nm over 10 s, holding that displacement for 10 s, and then unloading over 3 s. The elastic modulus was calculated by fitting the unloading force–displacement curve. Figures S5 and S6 (Supporting Information) present the load–displacement curves and the corresponding elastic modulus values. The measured elastic moduli were 63.5 ± 4.2 MPa for baseline Cu, 60.5 ± 6.8 MPa for W-Cu, 64 ± 2.9 MPa for Mg-Cu, and 58.9 ± 2.5 MPa for Mg/W-Cu. Since the 500 nm displacement exceeds the thickness of the sputtered layer, the measured elastic modulus reflects a combination of both the deposited material and the underlying bulk Cu. These results indicate that the thin metal coatings do not significantly alter the mechanical properties of the Cu substrate.

Electrochemical measurements were performed using polyether ether ketone (PEEK) cells with a two-electrode configuration. The working electrodes included modified Mg/W-Cu, Mg-Cu, W-Cu current collectors as well as baseline unmodified Cu. As a reference and counter electrode, an ≈100 µm thick Li metal disk with a diameter of 8 mm was employed. A wet ball-milled argyrodite-type Li_6PS_5Cl solid electrolyte (SE) was used as the separator. The electrochemical experiments were performed at room temperature and a stack pressure of ≈9 MPa. This stack pressure is on the lower end of the range reported in previous ASSB studies, either with Li foils or with Si anodes, with up to 20 MPa being employed.[63–65]

Figure 2 presents the electroanalytical results for the Li|SE|Mg/W-Cu, Li|SE|Mg-Cu, Li|SE|W-Cu, and Li|SE|Cu half-cells. Figure 2a,b compares galvanostatic electrodeposition profiles of modified and baseline current collectors in the initial and second cycles, tested at a current of 1 mA cm^{-2} with a fixed capacity of 1 mAh cm^{-2}. Figure 2c provides the Coulombic efficiency (CE) measurement during Li electrodeposition/dissolution. Figure 2d,e presents the cycling profiles and CEs at 1 mA cm^{-2}. Figure 2f–h offers galvanostatic profiles at selected time periods. Figure 2i shows the electrodeposition and electrodissolution overpotentials during cycling at the same testing condition. Per Figure 2a, all samples exhibit a distinctive "dip" at the onset of the profile during the first cycle, which is the nucleation overpotential for metal electrodeposition. Overpotential behavior during alkaline metal electrodeposition on nonalloying supports consist of two stages: Initially the voltage profile shows a sharp dip. This is followed by a plateau at a less negative voltage, with a slope of zero or that is weakly negative or positive. The plateau is present for the duration of the electrodeposition. The sharp dip is associated with crystallite layer nucleating on the support surface, while the subsequent plateau is associated with grain growth during film thickening. A slight negative slope is expected when grain growth becomes more facile as the film thickens, while a slight positive slope is expected when the opposite occurs. Such behavior is observed for Li electrodeposited on W-Cu and on baseline Cu working electrodes.

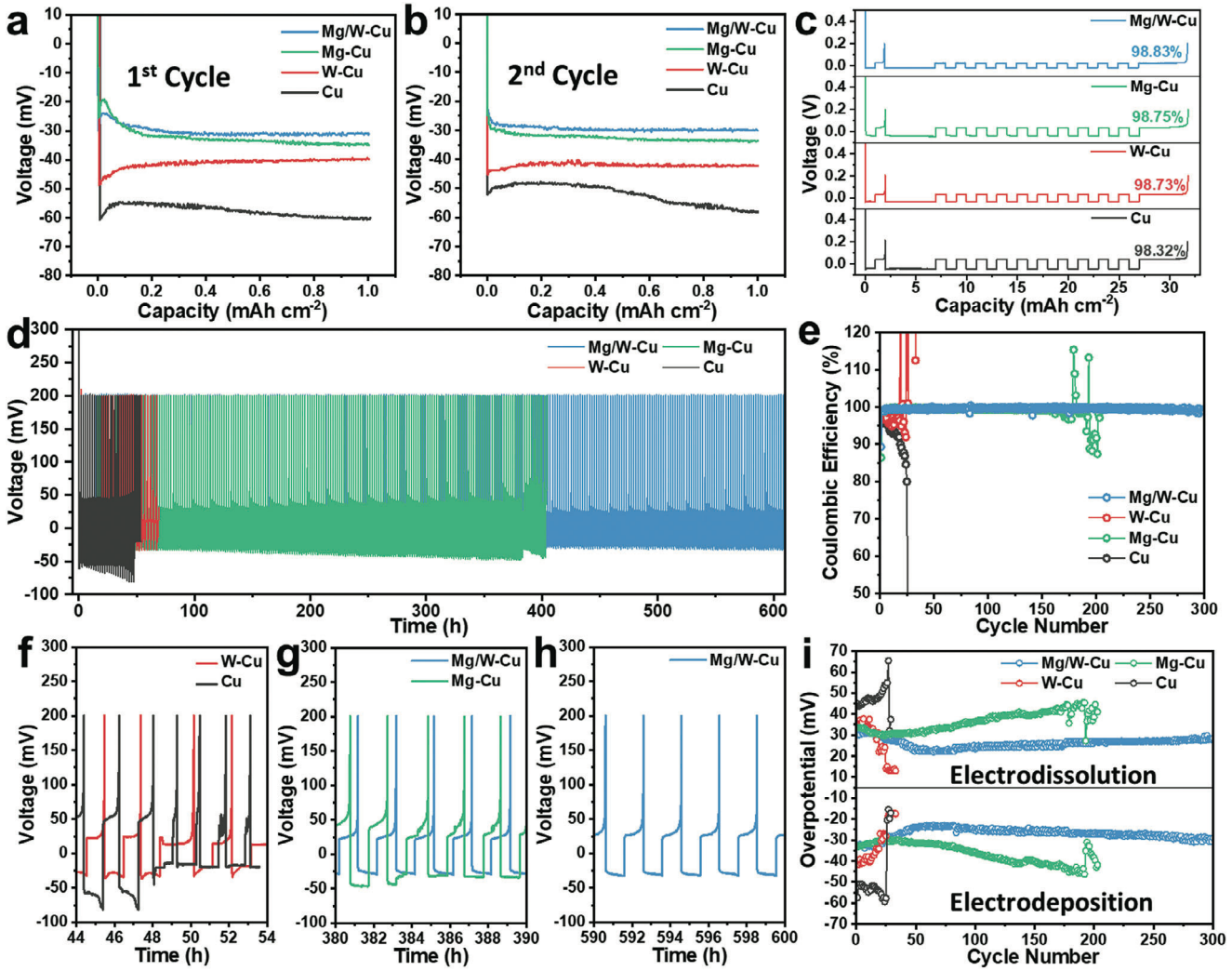

Figure 2. Electrochemical characterizations in asymmetric half cells using different current collectors, tested at 1 mA cm^{-2} to a fixed electrodeposition capacity of 1 mAh cm^{-2}. Galvanostatic electrodeposition profiles during a) 1st cycle and b) 2nd cycle. c) Coulombic efficiency measurement. d,e) Overall galvanostatic cycling performance with CE test. f–h) Representative galvanostatic profiles. i) Electrodissolution and electrodeposition overpotentials.

The other more complex electrodeposition voltage behavior consists of three stages. First there is the initial sharp dip, which is followed by a more gradual spike, which is then followed by a plateau. This behavior is observed with the Mg/W-Cu and Mg-Cu specimens. The nucleation overpotentials (initial sharp dip) are measured at 55 ± 7 and 47 ± 4 mV for baseline Cu and W-Cu, respectively. For Mg/W-Cu and Mg-Cu these values are 27 ± 3 and 28 ± 2 mV, respectively. The reduced nucleation overpotential on a Mg surface known for alloying supports such Li-Mg, Li-Au, and Li-Ag, being correlated with more facile nucleation kinetics and enhanced wetting.[66] The more gradual voltage spike is associated with an alloying reaction barrier between Mg and Li, leading to the formation of an extended Li-Mg solid solution. During electrodeposition, pure Li is deposited onto a Mg (and then Mg-Li alloy) surface, diffusing into the parent metal per its thermodynamic solubility. However, the alloying process is kinetically difficult due to the associated volume changes in the parent material and the stresses that results. The kinetic impediment to achieving the thermodynamically favored solid-solution is manifest as the observed voltage spike. This effect is quite apparent for electrodeposition/dissolution at a relatively high current density of 1 mA cm^{-2}. As stresses are relieved and the Li-Mg alloy is homogenized and diluted (increasing Li, constant Mg reservoir), the voltage spike decays into the terminal plateau.

Figure S7a (Supporting Information) shows the initial galvanostatic profile for the baseline Cu and W-Cu samples at a low current (0.05 mA cm^{-2}) between 0 and 1 V. It may be observed that there is negligible reversible or irreversible capacity, i.e., that Cu and W-Cu are inert with Li. It also indicates that during activation there is minimal SEI formed between the Li and the SE. Figure S7b (Supporting Information) shows the same activation protocol for Li|SE|Mg/W-Cu and Li|SE|Mg-Cu. In this case there is 0.23 mAh cm^{-2} of reversible capacities and an initial Coulombic efficiency (ICE) of 72%. The capacity loss is attributed to some irreversibility in the alloying of Li with Mg. For example the associated lithiation stresses may be physically damaging in the

Mg film, with limited pulverization, cracking or delamination.[67] Based on the Li-Mg phase diagram, Mg forms a random solid solution (α-phase with 0–15 at% Li) and an ordered solid-solution (β-phase with 30 at% Li and above).[68–71] Counting only the reversible capacity, the Mg layer alloys to $Li_{3.9}Mg$ (β-Mg), with the associated film swelling being in effect a volume summation of the inserted Li atoms.[72] For Li|SE|Mg-Cu, the reversible capacity achieved above 0 V is 0.17 mAh cm^{-2}, with an ICE of 66%.

Figure 2b shows the galvanostatic profiles of the half-cells in the 2nd cycle, where both Mg/W-Cu and Mg-Cu samples exhibit a notable absence of both the nucleation dip and the alloying spike. This is synonymous new film growth occurring epitaxially with the pre-existing Li-Mg alloy, thereby not requiring a distinct nucleation step at the onset. The alloying spike is absent since the material is a single phase. If distinct new Li grains were formed on the surface of the pre-existing Li-Mg alloy, a nucleation dip would have to occur, such as it did at cycle 1. At cycle 2 the nucleation overpotentials on the W-Cu and baseline Cu surfaces are 49 ± 3 and 41 ± 4 mV, respectively. With Li|SE|Mg/W-Cu and Li|SE|Mg-Cu, from cycle 2 onwards there is no discernable nucleation overpotential for Li electrodeposition. This indicates that the crystallites in the pre-existing Li-Mg intermetallic (that is not dissolved) serve as templates for further film thickening, possibly through an epitaxial process.

Figure 2c presents a comparative analysis of the CE during Li electrodeposition/dissolution process. The measurements were carried out following a standard protocol, as reported previously for evaluating the efficiency of Li deposition in liquid electrolytes.[73] The evaluation comprised three steps: First, an initial formation cycle was performed by electrodepositing Li at 1 mA cm^{-2} to a capacity of 1 mAh cm^{-2}, followed by electrodissolution at the same current to an anodic limit of 0.2 V. Secondly, a reservoir of 5 mAh cm^{-2} Li was electrodeposited at the same current, followed by ten cycles of electrodissolution/deposition (from that reservoir). Finally, the entire reservoir was electrodissolved to the 0.2 V anodic limit. The CE was calculated based on the cumulative electrodeposition and electrodissolution capacities from the reservoir. For Mg/W-Cu, Mg-Cu, W-Cu, and baseline Cu the calculated CEs are 98.83%, 98.75%, 98.73%, and 98.32%, respectively. The minimal difference of CEs (<1%) observed among these samples further supports negligible differences in the degree of early-stage capacity loss. This early loss, which is roughly equal in the four specimens, is due to SEI formation as well as electrochemically inactive "dead Li" that is formed on the collector surface. As will be demonstrated next, it is the longer-term cycling stability and the associated CE that are significantly influenced by the presence of the Mg and W layers on the Cu substrate.

Figure 2d–h compares the long-term cycling performance and CEs of Li|SE|Mg/W-Cu, Li|SE|Mg-Cu, Li|SE|W-Cu, and Li|SE-Cu half-cells, tested at a current density of 1 mA cm^{-2} with a Li electrodeposition/dissolution capacity of 1 mAh cm^{-2}. The bottom panels in Figure 2f–h display enlarged profiles of selected regions in Figure 2d. With a half-cell configuration the working electrode is an "empty" current collector. Since CE is never exactly 100%, an anodic cutoff voltage of 0.2 V is employed, after which the current is switched. Distinct differences in the voltage–time profiles are observed among the four working electrodes. Per Figure 2f with the baseline Li|SE|Cu and Li|SE|W-Cu cells deteriorate after 48 and 49 h (26 and 25 cycles), respectively. According to Figure 2g the Li|SE|Mg-Cu cell exhibits stable cycling up to 383 h (193 cycles), at which point a sudden voltage drop occurs, indicating a short circuit. Instability is also evident by the fluctuating CE values that start at the 193rd cycle. By contrast, the Li|SE|Mg/W-Cu cell demonstrates stable electrodeposition/dissolution for over 600 h (300 cycles) without any signs of deterioration. This is illustrated in Figure 2h. The accumulated electrodeposition/dissolution capacity reaches 300 mAh cm^{-2}. Since 1 mAh cm^{-2} of Li metal corresponds to ≈5 µm film, a cumulative 300 mAh cm^{-2} capacity corresponds to 1.5 mm of metal that is cumulatively electrodeposited and electrodissolved. Figure S8 (Supporting Information) shows the cycling performance for the Li|SE|Mg/W-Cu cell tested at a higher current of 2 mA cm^{-2} to 1 mAh cm^{-2}, maintaining a stable CE up to 200 cycles.

Figure 2i provides a comparison of Li electrodeposition/dissolution overpotentials during cycling, extracted from the 1 mA cm^{-2} to 1 mAh cm^{-2} results. For the baseline Cu cell, both electrodeposition/dissolution overpotentials gradually increase until a sudden drop in voltage occurs at the 26th cycle (48 h), indicating a short circuit. The cycle 1 electrodeposition/dissolution overpotentials are 57 and 45 mV, while cycle 25 overpotentials are 58 and 54 mV. It may be observed that W-Cu cell exhibits more stable and lower electrodeposition/dissolution overpotentials as compared to the baseline Cu, although a short circuit occurs nearly at the same cycle number. The cycle 1 electrodeposition/dissolution overpotentials are 41 and 35 mV, while cycle 25 overpotentials are 28 and 24 mV. It may be therefore concluded that the W layer by itself has a minimal effect on the cell's electrochemical stability but does allow for incrementally improved kinetics while the cell remains active. The Mg-Cu cell displays electrodeposition/dissolution overpotentials measured as 33 and 34 mV at cycle 1. Additionally, it demonstrates extended cycling stability for up to 193 cycles, with overpotentials being 46 and 45 mV before the onset of instability.

The Mg/W-Cu cell exhibits the lowest electrodeposition/dissolution overpotentials, being 32 and 30 mV at cycle 1. Even at cycle 300, the overpotentials remain low at 29 and 28 mV, underscoring its distinct electrochemical stability. Both Mg/W-Cu and Mg-Cu cells show a similar trend; decreasing overpotentials up to 50 and 30 cycles followed by an increase afterward. The initial overpotential decrease is likely associated with the enhancement of interfacial contact between the SE and current collector with repeated Li electrodeposition/dissolution.[32] As will be demonstrated, the subsequent overpotential increase is mainly attributed to the corrosion reactions at the SE-Li and SE-Cu interphases. For Mg-Cu the electrodeposition/dissolution overpotentials increase by ≈0.1 mV per cycle until the cell is short circuited. The overpotentials in the Mg-W/Cu cell is more stable, between 50 and 300 cycles the increase is 0.02 mV per cycle. The difference in overpotential increase rates between the Mg/W-Cu and Mg-Cu cells is associated with the difference in the corrosion resistance of the W coated versus the unmodified Cu surface.

Electrochemical impedance spectroscopy (EIS) analysis was conducted to further investigate changes in interfacial resistance during cycling. Figure S9 (Supporting Information) provides the Nyquist plots for Li|SE|Mg/W-Cu, Li|SE|Mg-Cu, and Li|SE|Cu cells. The cells were analyzed at cycle 1 through cycle 10, cycle

15, 20, 25, and 30, all tested at 1 mA cm^{-2} and 1 mAh cm^{-2}. Figure S10 (Supporting Information) extends the analysis for Li|SE|Mg/W-Cu, Li|SE|Mg-Cu, focusing on cycles 40 and higher. The plots were fitted using Z-view software with the corresponding results being detailed in Tables S1 and S2 in the Supporting Information. As shown in Figure S9d (Supporting Information), during cycles 1–10, all three cells exhibit a gradual decrease in bulk resistance (R_b), which stabilizes in subsequent cycles. This reduction is likely due to improved contact between cell components and the gradual densification of LPSCl under pressure during cycling. The calculated resistivity is the intrinsic resistance divided by the geometric contact area and multiplied by the geometric ionic path length (i.e., SE compact thickness). A reduction of the overall pore volume in the SE would result in an increase of effective contact area despite the geometric contact area being fixed, due to more SE contacting the electrodes. It would also result in a reduction in the effective path since ions have to diffuse around the pores, making their path more circuitous.

It should be noted that a large and sudden drop in R_b has been directly correlated with dendrite-induced short circuiting, the resultant dendrite being imaged by cryo-FIB SEM.[33] This sharp (rather than gradual) decrease in R_b is associated with electronic conduction through the 2D sheet-like metal dendrite becoming dominant, while ionic conduction through the SE becoming secondary. However, prior to the cell being short circuited, it is difficult to ascribe changes in R_b to dendrite motion per se. To understand the complex dendrite–impedance interrelations, authors have performed comprehensive analysis of the entire Nyquist plot, particularly considering the low-frequency region.[74–76] The interpretation of how dendrite motion through sulfide SE's affects the impedance response prior to short circuiting is further complicated by recent observations that dendrite growth occurs concurrently with SEI growth and with reactivity-induced pore formation.[32,33] These factors would influence the frequency response in several ways, including changes in the charge transfer resistance and in the SEI resistance.

The Li|SE|Mg/W-Cu cell displays an initial bulk resistance (R_b) of 54.0 Ω and a combined SEI and charge-transfer resistance (R_{SEI} + R_{ct}) of 6.2 Ω. With cycling the R_b gradually decreases, becoming 50.5 Ω at cycle 30. The R_{SEI} + R_{ct} value remains stable, being 6.2 Ω at cycle 30, with some fluctuations in between. This indicates that at these cycle numbers the cell interphases undergo minimal degradation. The interface stability with Mg-Cu is not as good, with R_{SEI} + R_{ct} going from 5.8 Ω at cycle 1–9.1 Ω at cycle 30. In the Li|SE|W-Cu cell, the initial R_b measures 89.0 Ω, which decreases to a lower value of 57.0 Ω by cycle 30. The R_{SEI} + R_{ct} starts at 28.2 Ω at cycle 1 and increases slightly to 30.0 Ω after 30 cycles. The R_{SEI} + R_{ct} for the baseline Cu cell increases significantly with cycling, to a point where by cycle 5 it is possible to separate R_{SEI} + R_{ct} into two distinct overlapping semicircles, the R_{SEI} being at the higher frequency. At cycle 1 R_{SEI} + R_{ct} for the baseline Cu is 13.6 Ω. By cycle 5 the semicircle R_{SEI} is 9.2 Ω, while the semicircle R_{ct} is 72.8 Ω. Both R_{SEI} and R_{ct} continue to increase, reaching 18.7 and 90.1 Ω by cycle 30. Figure S10 and Table S2 (Supporting Information) present the Nyquist plots and associated fitting results for the extended cycling of the Mg/W-Cu and Mg-Cu specimens. The Li|SE|Mg-W/Cu cell exhibits a relatively stable R_b throughout the cycling up to 300 cycles, with some fluctuations. For instance, R_b measures 51.0, 50.1, 52.2, and 53.2 Ω at cycles 40, 140, 240, and 300, respectively. Additionally, the R_{SEI} + R_{ct} exhibits a slightly increasing trend, measuring 5.6 Ω at cycle 40, 8.0 Ω at cycle 140, 7.2 Ω at cycle 240, and 7.4 Ω at cycle 300. In the Li|SE|Mg-Cu cell, both R_b and R_{SEI} + R_{ct} demonstrate an increasing trend, measuring 60.6 and 8.8 Ω, 67.2 and 13.1 Ω, 78.2 and 18.0 Ω, at cycle 40, 140, 240, respectively.

To investigate the impact of Mg and W layer thicknesses on electrochemical performance, four additional specimens were prepared. The sample that is the primary focus of this work is 140 nm Mg/30 nm W (Mg/W-Cu). The samples used for this study are 5 nm Mg/30 nm W (5Mg/W-Cu), 50 nm Mg/30 nm W (50Mg/W-Cu), 140 nm Mg/5 nm W (Mg/5W-Cu), and 140 nm Mg/100 nm W (Mg/100W-Cu). Figure S11a presents the cycling performance of Mg/5W-Cu and Mg/100W-Cu in half-cells. The Mg/5W-Cu cell, with a thinner 5 nm W coating, shows significant CE fluctuations after 215 cycles, though it performs slightly better than the Mg-Cu cell without the W coating. In contrast, the Mg/100W-Cu cell, with a thicker 100 nm W coating, demonstrates stable cycling up to 300 cycles. This indicates that a 5 nm W coating is insufficient to protect the Cu from corrosion, likely due to incomplete surface coverage, pinhole defects, microcracks etc. Conversely the 100 nm W layer provides comparable protection to a 30 nm layer, albeit with added weight and with higher deposition cost. Figure S11b (Supporting Information) compares the performance of Mg/W-Cu collectors with different Mg thicknesses. The 5Mg/W-Cu sample exhibits fluctuating CE from the onset, while the 50Mg/W-Cu specimen demonstrates stable cycling for up to 78 cycles before cell failure. The worse performance of the 5 nm Mg layer is likely due to more rapid physical degradation of the film, at the activation step and during subsequent electrodeposition/dissolution cycling. To take up the same amount of Li atoms into a solid-solution, a 5 nm Mg layer will expand approximately ten times more than a 50 nm Mg layer would. This generates much greater stress levels at every cycle, leading to accelerated pulverization. The as-deposited 50 nm Mg layer may also display incomplete surface coverage and may be cracked and contain pinholes from the onset. Combined these factors would lead to a reduction in cell's electrochemical stability. While a sufficient Mg and W film thickness is necessary to achieve stable cycling performance, there are practical limits to how thick the films can be. With increasing thickness, the thin films will be more stressed (especially the refractory W), and will be more costly to sputter deposit onto the Cu substrate. Thicker layers will also add weight and volume to the cell, without increasing reversible capacity.

The SEI layer formed by the reduction of Li_6PS_5Cl by the Li is well known, having terminal products such as Li_2S, Li_3PS_4, Li_3P, and LiCl.[28] However, it is not the only SEI formed in the negative electrode during cycling and/or storage. Therefore it will be termed SEI-1, keeping it distinct from SEI-2 which forms through the reaction of Li_6PS_5Cl with the Cu current collector. **Figures 3** and S12 (Supporting Information) display cross-sectional cryogenic focused ion beam (cryo-FIB) SEM and associated energy-dispersive X-ray spectroscopy (EDXS) microstructural analysis of post-electrodeposited and post-electrodissolved Li|SE|Mg/W-Cu cells. All tests were conducted at a current of 1 mA cm^{-2}. Figure 3a–c presents the cell microstructure

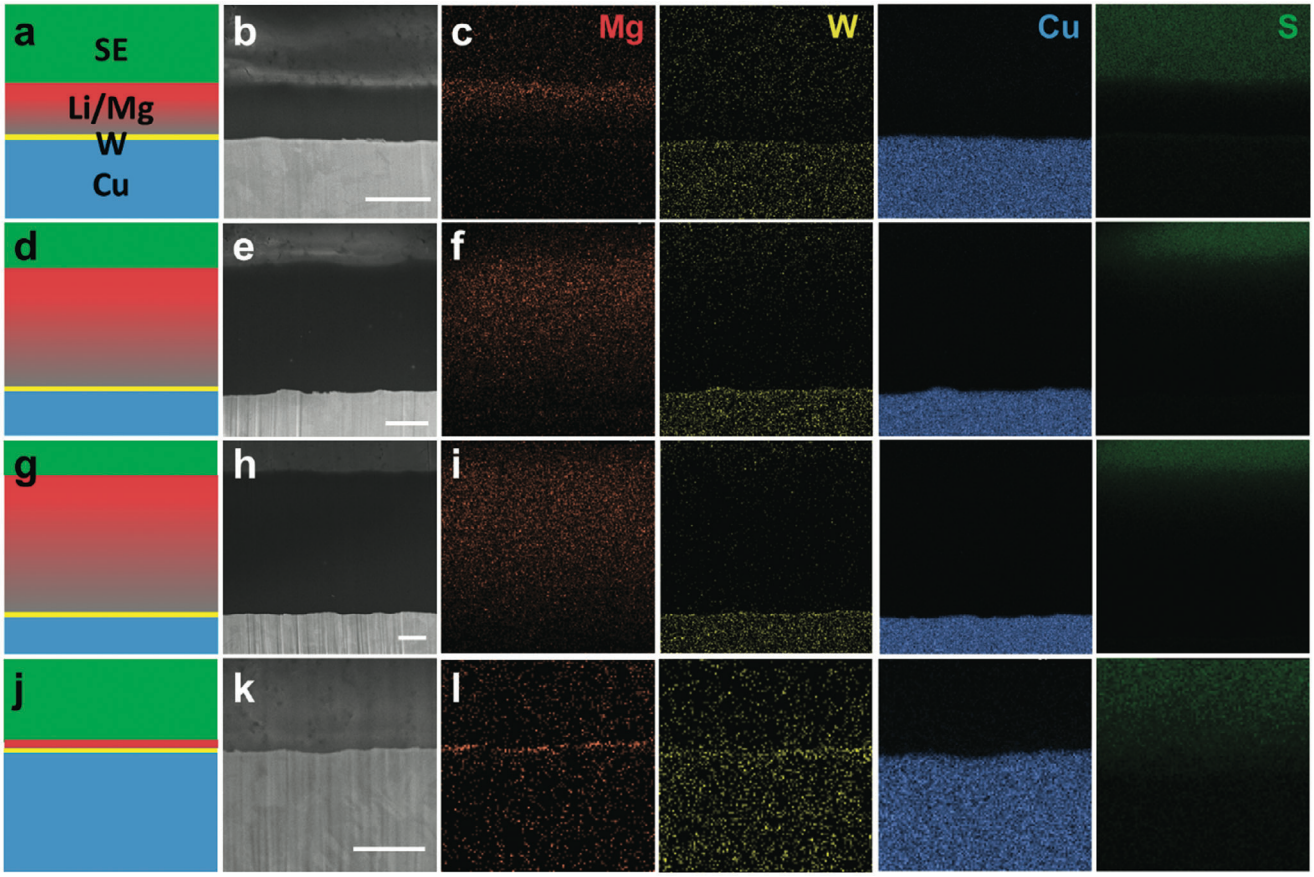

Figure 3. Cryo-FIB cross-sectional SEM and EDXS of Li|SE|Mg/W-Cu cells, tested at 1 mA cm^{-2}. a–c) Electrodeposition of 1 mAh cm^{-2}, d–f) electrodeposition of 3 mAh cm^{-2}, g–i) electrodeposition of 5 mAh cm^{-2}, j–l) electrodissolution to 0.2 V. The scale bar is 5 µm.

after electrodeposition of 1 mAh cm^{-2}. Figure 3d–f displays the cell microstructure after electrodeposition of 3 mAh cm^{-2}. Figure 3g–i shows it after electrodeposition of 5 mAh cm^{-2}. Figure 3j–l displays the microstructure after electrodissolving the remaining Li to the 0.2 V anodic limit. Figure S12 (Supporting Information) shows the EDXS line scan of the cell cross-sections at corresponding electrodeposition/dissolution conditions. Schematics representing the cell structure are provided in front of each row with the following color schemes: SE (green), Li/Mg solid solution (grey/red), W (yellow), and Cu (blue). At accumulated capacities of 1, 3, and 5 mAh cm^{-2}, the measured metal thickness is 4.4, 14.6, and 24.2 µm, comparable to the theoretical values of 4.9, 14.7, 24.5 µm, respectively. The electrodeposited Li at 1 mAh cm^{-2} is observed to be largely free of pores and of imbedded SEI. This Li microstructure remains consistent after accumulating capacities of 3 and 5 mAh cm^{-2}.

Further evaluating the Li|SE|Mg/W-Cu cells microstructure, it may be observed that within the resolution of the EDXS area and line scans the alloying of Li with Mg in nonuniform. In the 1 mAh cm^{-2} specimen the region of the Li-Mg film facing the W underlayer shows reduced Mg signal intensity relative to the region facing the SE. This indirectly indicates that Li is segregated to that interface. As shown in Figures S13 and S14 (Supporting Information), early stage segregation of Li toward the current collector is also present in the Li|SE|Mg-Cu specimens. These figures present analysis of the Li|SE|Mg-Cu cells, illustrating cell microstructures after electrodeposition of 3 mAh cm^{-2}, electrodeposition of 5 mAh cm^{-2} and electrodissolution to the 0.2 V anodic limit. Figure S14 (Supporting Information) provides the EDXS line scan scans at these test conditions. At accumulated capacities of 3 and 5 mAh cm^{-2}, the electrodeposit remains uniform and free from pores and embedded SEI.

The room temperature diffusivity of Li in Mg is about an order of magnitude lower than Li self-diffusion ($\approx 10^{-11}$ vs 10^{-10} cm^2 s^{-1}).[77–79] Moreover it has also been reported that the ongoing alloying/dealloying process for Li_xMg is somewhat sluggish at the higher electrodeposition/dissolution rates.[78] This would result in a kinetically-driven effect during electrodeposition where Li in the Li_xMg alloy is segregated towards the interface with the SE. The opposite is observed during early stage of electrodeposition with both the Mg/W-Cu and Mg-Cu collectors. We propose that shear stress effects are responsible for creating this distinct Li concentration gradient in Li_xMg, one that is opposite to what is expected from diffusivity differences. However before advancing to understand the role of stress in driving segregation, we will consider the role of diffusivity by itself. The details of the models used for **Figure 4** are provided in the Supporting Information. Figure 4a–c examines the effect of Li diffusivity on the Li transport, concentration gradients, and the utilization of

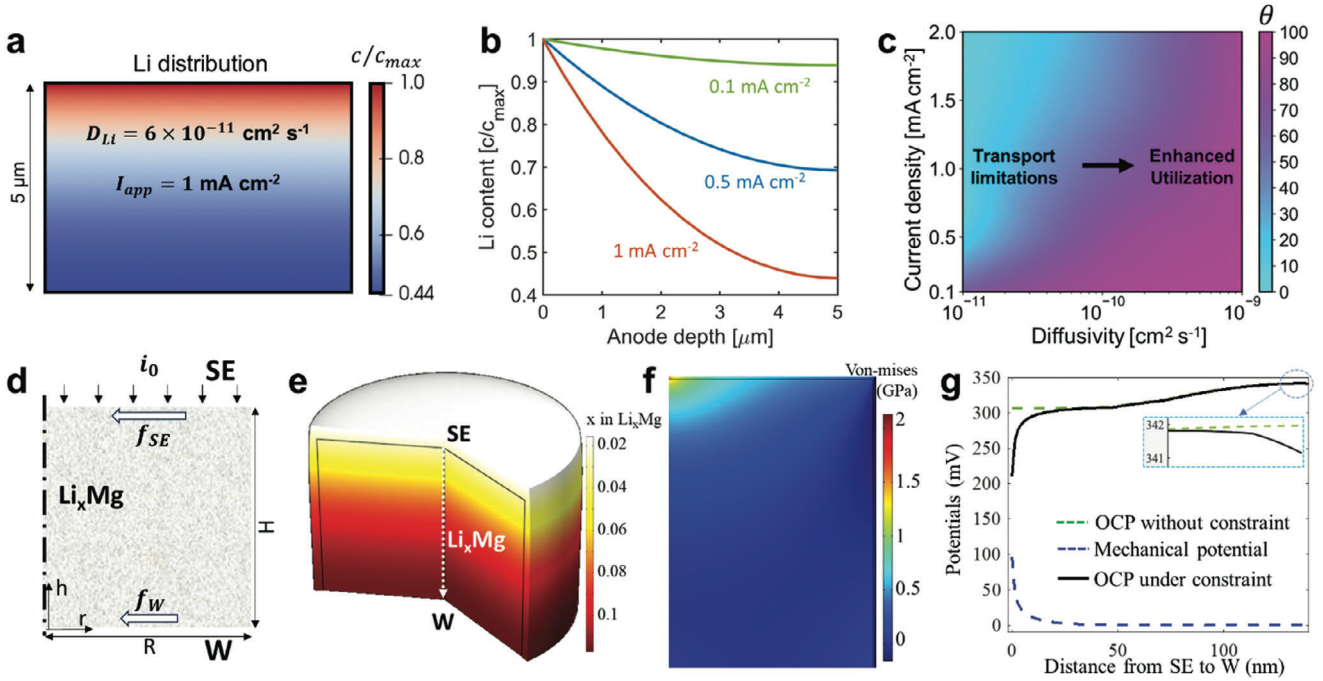

Figure 4. a) Li distribution within the 5 μm thick substrate (Li-Mg alloy) for diffusion coefficient and current density of 6×10^{-11} cm^2 s^{-1} and 1 mA cm^{-2} , respectively. b) Effect of current density on Li distribution profiles. c) Utilization (θ) of the substrate (Li-Mg alloy) as a function of Li diffusivity and current density. d) Schematics of the Li_xMg layer under lateral shearing from the SE and W layer and constant current density from the SE. e) The spatial distribution of Li molar fraction x in the Li_xMg particle within the first 10 s. f) The equivalent von-mises stress distribution after charging for 10 s. g) The potential as a function of the distance from the SE to the W. The dashed green line represents the Li open-circuit potential without mechanical constraint. The dashed blue line represents the mechanical potential, or the strain energy due to the stress state in (f). The solid black line represents the total Li open-circuit potential under mechanical constraint, which is the summation of the two dashed lines.

the substrate using a mesoscale model. It is assumed that there are no interfacial stresses. Figure 4a shows the Li concentration profile for a 5 μm thick substrate at an applied current density of 1 mA cm^{-2} and Li diffusivity of 6×10^{-11} cm^2 s^{-1}. Here, the diffusion process is simulated until the Li concentration reaches its maximum value (69.6 mmol cm^{-3} for Li-Mg alloy) at the top surface of the substrate. After this instance in the Li deposition process, Li can potentially deposit at the top of the substrate, marking the onset of interface instability.

Figure 4b shows the Li concentration through the anode depth for different current densities (0.1, 0.5, and 1 mA cm^{-2}). It is observed that significant concentration gradients arise with an increase in current density from 0.1 to 1 mA cm^{-2} owing to the sluggish Li transport. Such a phenomenon will result in significant underutilization of the alloy near the current collector, which is the opposite of what is observed. Figure 4c shows the effect of Li diffusivity on the substrate utilization (i.e., the degree of lithiation achieved) for different applied current densities. The performance is observed to improve greatly with the Li diffusivity, suggesting that the high Li diffusivity within the alloy can contribute towards enhanced rate capability, while maintaining stable Li metal/SE interface. It is important to note that this analysis, which is based on the Li diffusivity of the substrate does not explain the trends observed in the experiments. Specifically, the Li content after the electrodeposition is observed to increase from SE to the current collector, whereas the diffusion model predicts the opposite. This discrepancy between the experimental and modeling trends suggests that the lithiation dynamics is not solely dependent on the Li diffusivity within the Li-Mg alloy and the chemo-mechanical effects play an important role.

Rather than being driven by diffusivity differences, the initial Li segregation towards the W (or Cu) interface is a stress-driven effect. It originates from the different interfacial adhesion of the SE-Li_xMg and the Li_xMg-W interfaces, the former being mechanically coupled through the reacted SEI-1 layer. During electrodeposition, the Li_xMg alloy increases in volume proportionally to the Li content. This creates a mixed stress state at the SE-Li_xMg interface, the shear stresses driving the segregation behavior. For Li_xMg-W or the Li_xMg-Cu interface shear stresses are not generated since the interface is free to slide as the Li_xMg alloy widens. An electro-chemo-mechanical model was developed to further understand this effect, using SE-Li_xMg-W as the targeted system. The interfacial friction (also known as lateral adhesion) was found positively correlates with the surface adhesion energies of contacting layers. An adhesion energy of 1 J m^{-2} would lead to an accumulated interfacial friction up to 1 GPa with non-negligible change to the open-circuit potential up to 100 mV.[80,81] Figure 4d–f provides a quantitative description on this effect after the initial lithiation of a plate-like *bcc* Li_xMg particle for half minute. It is assumed that the Li_xMg plate has an initial thickness of $H_0 \approx 140$ nm and an initial radius of $R_0 \approx 100$ nm. A simplified model in Figure 4d shows the cross-section of one such Li_xMg plate, with half of it being shown. Figure 4e shows the

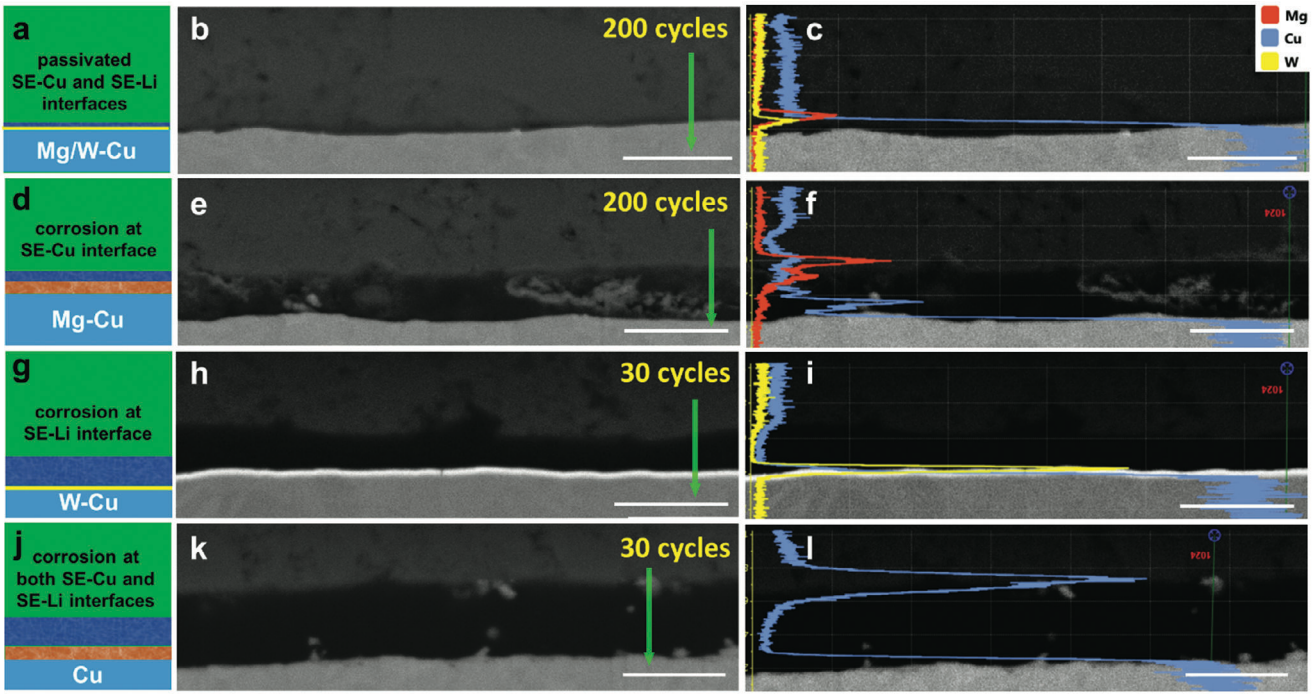

Figure 5. Cryo-FIB cross-sectional SEM and linear EDXS analysis of asymmetric cells at the fully electrodissolved state after cycling at 1 mA cm^{-2} to 1 mAh cm^{-2}. a–c) Li|SE|Mg/W-Cu cell after 200 cycles, d–f) Li|SE|Mg-Cu cell after 200 cycles, g–i) Li|SE|W-Cu cell after 30 cycles, and j–l) Li|SE|Cu cell after 30 cycles. The scale bar is 5 µm.

spatial distribution of Li molar fraction x in the Li_xMg after lithiation for $t = 30$ s. The Li diffusivity in *bcc* Li_xMg is taken as $D_{Li} \approx 10^{-11}$ cm^2 s^{-1}.[78]

As the plate gradually expands ($R > R_0$) during lithiation, its internal strain/stress accumulates due to the different Li concentration difference and frictions from the SE and the W layer. Figure 4f presents the von-mises stress distribution of the cross-section. The developed stress reaches a maximum of 2 GPa at the SE side, with a gradient toward the W side to 0.02 GPa. This stress/strain state causes a considerable strain energy accumulation, which further modifies the Li open-circuit potential substantially, as shown in Figure 4g. The Li open-circuit potential (OCP) under mechanical constraint is the sum of Li OCP without constraint ($-\mu_{Li}/F$) and the mechanical potential (E_ϵ/F, with E_ϵ being the stored strain energy). The value of $-\mu_{Li}/F$ as a function of x in Li_xMg is provided in Figure S15 in the Supporting Information. It is 307 mV when $x = 0.17$ (corresponds to Li content near the SE side) and 342 mV when $x = 0.06$ (corresponds to Li content near the SE side). This alloying composition driven potential difference (35 mV) would drive segregation of Li away from the SE interface and towards the W (or the Cu) interface. Lithium segregation away from the SE would be further promoted by the potential difference (96 mV) originating from the chemo-mechanical stress effects. What the model indicates is that there is a kinetic difficulty for electrodepositing Li near the SE-Li_xMg interface. The SEI layer keeps it mechanically coupled and results in shear stresses. The Li atoms diffuse into the bulk Li_xMg and segregate toward the Li-W (or Li-Cu) interface instead. Qualitatively this is analogous to the stress-driven segregation reported by Tu and Ceder for Li-Ag compounds.[82]

Figures 5 and S16 (Supporting Information) provide the cross-sectional cryo-FIB SEM and EDXS line scan spectra of the microstructural analysis of post-cycled half-cells cells employing Mg/W-Cu, Mg-Cu, W-Cu, and baseline Cu current collectors. Due to its sensitivity to elements with varying atomic number, backscattered electron (BSE) imaging was utilized to study the interphases between Li and SE. All cells were cycled at 1 mA cm^{-2} to 1 mAh cm^{-2} with an anodic limit of 0.2 V. Figure 5a–c,d–f shows the Mg/W-Cu and Mg-Cu cell microstructures at the electrodissolved state after 200 cycles. Figure 5g–i,j–l present the microstructures of W-Cu and baseline Cu cells at the electrodissolved state after 30 cycles. Additionally, Figure S16 (Supporting Information) displays the Mg/W-Cu cell microstructure at the electrodissolved state after 30 cycles, electrodeposited state after 300 cycles, and electrodissolved state after 300 cycles. Schematics representing the cell microstructures after cycling are provided in front of each row.

As shown in Figure 5a–c, uniform Li electrodeposition/dissolution was observed for the Mg/W-Cu cell after 200 cycles without noticeable pores and electrolyte or current collector fragments. Of course the LPSCl SE still reacts to some extent with the Li in the Li-Mg alloy. However the kinetics of this parasitic reaction are markedly suppressed. In parallel the W effectively eliminates the corrosion of the Cu by the LPSCl, at least as long as it maintains physical integrity on the collector surface. As expected, EDXS analysis indicates that the Mg layer is recovered after full electrodissolution. Figure S16c–d,e,f (Supporting Information) provides additional analysis of the electrodeposition and electrodissolution behavior, after 300 cycles at 1 mA cm^{-2} to 1 mAh cm^{-2}. The electrodeposit

morphology remains uniform as it forms a Li-Mg solid solution. There are no discernable W signals originating from the alloy, agreeing with phase diagram data that shows minimal Li-W and Mg-W miscibility and no known ternary compounds. In the electrodissolved state, there is minimal corrosion products present. The EDXS line scan results highlight the stability of the unreactive W layer. In summary, the W layer remains attached to the Cu surface at all testing conditions, while the Mg layer reversibly alloys and dealloys with the Li. After complete electrodissolution there is no obvious presence of dead metal or clump-like SEI. Rather the Mg/W layer reverts to its original geometry, with the W facing the Cu and the Mg facing the SE.

The microstructure of the Mg-Cu cell after 200 cycles is presented in Figure 5d–f. At the interface between the SE and Cu collector there is a dark contrast layer interspersed with numerous detached brighter particles. EDXS line scan spectra reveal strong Cu signals in these particles while Mg is mostly concentrated in the SE interface, indicating that a single Mg layer is not fully effective in protecting the Cu from reacting with the SE. During repeated alloying–dealloying, the associated volume changes and stresses will cause cracking and local pulverization of the Mg layer. This may also lead to the layer's partial detachment from the collector surface during extended cycling. Shear stresses generated during lithiation/delithiated of Li_xMg were presented in Figure 4. Such stresses would drive cycling-induced cracking in the delithiated Li_xMg layer. Aided by the 9 MPa external stack pressure, the SE comes into contact with the Cu collector at the break points in the Mg layer to form SEI-2. Without the Mg layer the formation of SEI-2 is accelerated since Cu directly contacts the SE at every 100% depth-of-discharge (DOD). Since Mg undergoes cycling-induced damage, it cannot fully prevent this reaction from occurring with extended cycling. The corrosion of the Cu by the LPSCl to form SEI-2 and the role of W in preventing this will be detailed later in the manuscript.

Figure 5g–i illustrates the microstructural analysis of W-Cu after 30 electrodeposition/dissolution cycles, shown in the electrodissolved state after the cell obtained the 0.2 V anodic cutoff limit. The BSE image reveals a very thin, bright layer of W closely adhered to the Cu surface, with no evidence of detached particles. EDXS analysis confirms that the sputtered W layer remains conformal and intact after cycling, effectively protecting the Cu from corrosion. It may also be observed that interface between the SE and the current collector is filled with inactive Li metal. Li displays a darker contrast in back scattered mode imaging as compared to the denser LPSCl. This result indicates that the W layer is effective in protecting the Cu from corrosion by the sulfide. However, it does not mitigate issues related to nonuniform Li electrodeposition/dissolution (due to poor wetting), as indicated by the relatively low CE of the half-cells.

Figure 5j–l provides the microstructural analysis of the baseline Cu cell after 30 cycles. The cross-sectional BSE image reveals a corrosion layer consisting of multiple phases with varying contrast. The EDXS results show a strong Cu signal in the brighter particles, which appear to be the corrosion products. Additionally, a relatively thick layer of inactive Li metal is present between the SE and the collector, being attributed to the poor wetting of Li on the Cu surface. Without the W or the Mg, both Li/SE (SEI-1) and SE/Cu (SEI-2) reactivity is ongoing, while wetting is poor. This explains the lowest electrochemical stability of all specimens in the baseline Cu.

To further understand the role of the W layer in preventing SEI-2, static corrosion experiments were performed at room temperature and at 60 °C, comparing baseline Cu and W-Cu symmetric cells. The relevant 9 MPa external pressure was employed, but the cells were not electrically connected. Figure S17 (Supporting Information) shows digital photographs of the Cu current collectors after 1, 4, and 7 d at room temperature and at 60 °C. At room temperature the Cu surface noticeably changes in color after the 4 d hold, indicating macro-scale corrosion of the Cu surface by the LPSCl. The amount of corrosion product increases after the 7 d hold. As expected, the corrosion reaction is significantly accelerated at elevated temperatures. At 60 °C the Cu foil is heavily reacted after even 1 d, being further corroded by day 4 and day 7. There is no evidence of surface passivation with prolonged exposure, indicating that the formed sulfides are not kinetically protective. In contrast, Figure S18 (Supporting Information) shows the W-Cu foil held at 60 °C. Even after 7 d there is no macroscopically discernable corrosion of the collector surface. Thermodynamically, the W layer will react with LPSCl to form WS_2.[83] However due to the low diffusivity of W at 60 °C (corresponding to homologous temperature 0.08549) this reaction is kinetically limited.

Next, microstructural analysis was performed on these two types of collectors. Figures S19 and S20 (Supporting Information) present top-down and cross-sectional FIB-SEM images and the EDXS maps of the baseline Cu cell that was held at room temperature. For milling the cross-sections, a protective Pt layer is present on the sample surface. Figures S21–S22 and S24–S25 (Supporting Information) show this analysis for baseline Cu and W-Cu, held at 60 °C. Figure S23a provides an average thickness of the corrosion layer for the baseline Cu; measuring 62 nm at day 1, 83 nm at day 4, and 462 nm at day 7. At 60 °C these values are 243, 2005, and 2337 nm, respectively. Figure S22 (Supporting Information) presents the corresponding EDXS line scan spectra at the baseline Cu cross-sections, indicating these layers primarily consists of Cu, S, and O signals, suggesting compositions such as copper sulfide, copper oxide, and copper sulfate. In addition, multiple layers within the corrosion region are evident, as reflected by the contrast difference. Figures S24 and S25 (Supporting Information) present an analogous corrosion study with the W-Cu sample at 60 °C. It is evident that the surface of W-Cu remains microscopically smooth. There are minimal signs of surface corrosion, such as pitting or secondary phase formation. Per EDXS line scan there is also no evidence (as expected) of physical intermixing of the two layers.

AF-ASSBs will experience high anodic voltages as a result of Li exhaustion if the cells were overdischarged. This will place a high oxidative voltage on the interface of the "empty" current collector and the SE. Since conventional LIBs do not contain a secondary Li reservoir at the anode either, the Cu collector surface is known to corrode in the overdischarged state.[84,85] This is the primary reason why LIBs are not fully discharged in practice. The oxidative electrochemical stability of the four current collectors against LPSCl SE was evaluated in symmetric configurations, without the presence of Li metal. These cells are labeled Mg/W-Cu|SE|Mg/W-Cu, Mg-Cu|SE|Mg-Cu, W-Cu|SE|W-Cu, and Cu|SE|Cu. This was done by holding the cells at 4.2 V.

Figure S26a (Supporting Information) presents the corrosion currents observed in different samples held at 4.2 V for up to 100 h, with selected regions detailed in Figure S26b–d in the Supporting Information. All cells initially exhibit a rapid drop in the anodic current, followed by stabilization. After 10 h for Cu|SE|Cu, W-Cu|SE|W-Cu, Mg-Cu|SE|Mg-Cu, and Mg/W-Cu|SE|Mg/W-Cu, the currents are 39, 3, 3, and 4 μA, respectively. After 50 h these values are 35, 3, 2, and 2 μA. After 90 h they are 16, 2, 1, and 1 μA. This indicates that at all stages of the test the baseline Cu collector corrodes the most, while the Mg-Cu|SE|Mg-Cu and Mg/W-Cu|SE|Mg/W-Cu corrode the least. However, as indicated by cryo-FIB SEM analysis, electrochemical cycling damages the integrity of a single Mg layer, allowing corrosion products to accumulate during cycling. Therefore, a bilayer Mg/W approach is necessary to ensure long-term cell stability through a range of conditions.

The reactivity of Mg-Cu, W-Cu, and baseline Cu current collectors against sulfide SE was further investigated by XPS characterization, sampling approximately top 5 nm of the specimen surface. To investigate the chemical stability, these current collectors were pressed onto sulfide SE and left undisturbed for 48 h without an applied voltage. Subsequently, they were separated from the SE and subjected to the XPS analysis. All cells were disassembled in an Ar-filled glove box and transferred to XPS analysis chamber using a dedicated holder to avoid exposure to air. As has been demonstrated, the Cu support is significantly corroded by the SE. However this underlying corrosion layer will not show up in XPS analysis since it samples only the top ≈5 nm of material.

Figure S27a,b (Supporting Information) presents the results for the samples held for 48 h without cycling, showing high-resolution S 2p and Li 1s spectra. A key difference is observed in the baseline Cu, which exhibits stronger S signals than that of Mg/W-Cu, Mg-Cu, and W-Cu samples. There are three pairs of S 2p peaks for the Cu sample, corresponding to Li_2S (160.4 eV (S $2p_{3/2}$) and 161.6 eV (S $2p_{1/2}$)); Li_6PS_5Cl (161.2 eV (S $2p_{3/2}$) and 162.4 eV (S $2p_{1/2}$)); and SO_x (166.9 eV (S $2p_{3/2}$) and 168.1 eV (S $2p_{1/2}$)). The dominant Li_2S signal originates from the decomposition of the sulfide SE, which appears to be catalyzed by its physical contact with the Cu. By contrast, the surfaces of Mg/W-Cu, Mg-Cu, and W-Cu samples lack Li_2S signals, with weak peaks attributed to the trace amount of residual electrolyte. The Li 1s spectra further support the relatively strong Li signals (Li_2S and Li_2O) on the Cu surface, in contrast to the absence of Li signals on the Mg/W-Cu, Mg-Cu, and W-Cu surfaces. A separate set of XPS experiments was focused on interface stability during electrodeposition/dissolution. A fixed capacity of 1 mAh cm^{-2} Li was electrodeposited onto the surface at 1 mA cm^{-2}, followed by electrodissolving to an anodic limit of 0.2 V. Figure S27c,d (Supporting Information) provides the S 2p spectra after 1 and 10 cycles. By cycle 10, all samples show an increasing Li_2S peak ratio, with 14% for Mg/W-Cu, 19% for Mg-Cu, 27% for W-Cu, and 43% for the baseline Cu. A higher Li_2S content typically indicates more pronounced electrolyte decomposition, likely due to the corrosion of Li metal and/or the Cu collector. The introduction of Mg and W coatings significantly reduces electrolyte decomposition and helps stabilize the interface. Since the current collector must be physically peeled from the SE to expose the interface for XPS measurements, separating them after extended cycling appears to introduce significant specimen preparation-related artifacts. Because of this concern, interfacial analysis between the SE and different current collectors is not presented for longer cycle numbers.

The thermodynamic reaction energy diagram shown in Figure S28 (Supporting Information), considers the reactivity between the Li-Mg alloy or pure Li/Mg and Li_6PS_5Cl. This analysis was performed using Materials Project database.[86] It may be observed that the reaction energy becomes less negative (lower driving force) as Li is alloyed with Mg. This explains the reduced reactivity of the Li-Mg layer versus pure Li, especially at low electrodeposit thickness where the film is Mg-rich. However, Mg by itself is insufficient for achieving extended electrochemical stability because it cannot fully prevent the SE from contacting and reacting with Cu current collector. This occurs near 100% DOD when most of the Li is electrodissolved. As was demonstrated, with cycling the Mg loses its full conformality with the Cu support, allowing for contact points where Cu and LPSCl will react to form SEI-2 based on mixed copper sulfides. Copper sulfides (CuS and Cu_2S) are known for their favorable electrical conductivity, ranging from 30 to 2400 S cm^{-1} for CuS and Cu_2S.[87–90] In fact, copper sulfides have been considered as potential cathode materials due to these electrical and ionic conduction properties and their high voltage reversibility (likely not relevant for anode voltages).[91] Being a mixture of copper sulfides, SEI-2 is a good electronic conductor and a reasonable ionic conductor, and is therefore highly deleterious to the electrochemical stability of the sulfide-based AF-ASSBs. As was shown, rapid formation of copper sulfides does not require an external voltage. The Cu foils were extensively corroded by the S species in LPSCl while in storage. The refractory W blocking layer has a positive influence on the electrochemical stability of cells by preventing the formation this SEI-2. According to the equilibrium binary phase diagram, W does form sulfides WS_2 and WS_3.[83] Tungsten is refractory (T_m = 3422 °C, highest of any element) and is known to be kinetically resistant to various forms of sulfidic corrosion at room temperature. The W layer is also thermodynamically stable against Li and against Mg, having minimal mutual solubility at room temperature and not forming intermetallic phases.[92]

To broaden the methodology of using a refractory metal-based underlayer to stabilize SEI-2, molybdenum (T_m = 2623 °C) and niobium (T_m = 2477 °C) films were examined. Just as with the W layer, 30 nm thick Mo or Nb layers were sputter deposited onto the Cu collector along with 140 nm Mg layer on top of them. These samples are denoted as Mg/Mo-Cu and Mg/Nb-Cu, respectively. Figure S29a,b (Supporting Information) shows the electrochemical cycling performance of these samples, measured in half-cells at 1 mA cm^{-2} to 1 mAh cm^{-2}. Both Li|SE|Mg/Mo-Cu and Li|SE|Mg/Nb-Cu cells exhibit stable cycling up to 300 cycles without any signs of failure. This result indicates that the design concept is broadly applicable to other refractory metal coatings, which effectively prevent Cu corrosion and stabilize the SEI-2 layer. A nonrefractory metal coating of tin (T_m = 232 °C) was also fabricated using a similar approach, and the sample being labeled Mg/Sn-Cu. Figure S29c (Supporting Information) presents the cycling performance of the Li|SE|Mg/Sn-Cu cell, which remained stable for 200 cycles before the CE begins to deteriorate. This performance is not significantly better than that of the Li|SE|Mg-Cu cell. The diminished performance of the Sn-coated sample is likely due to the formation of Li-Sn alloys, which experience

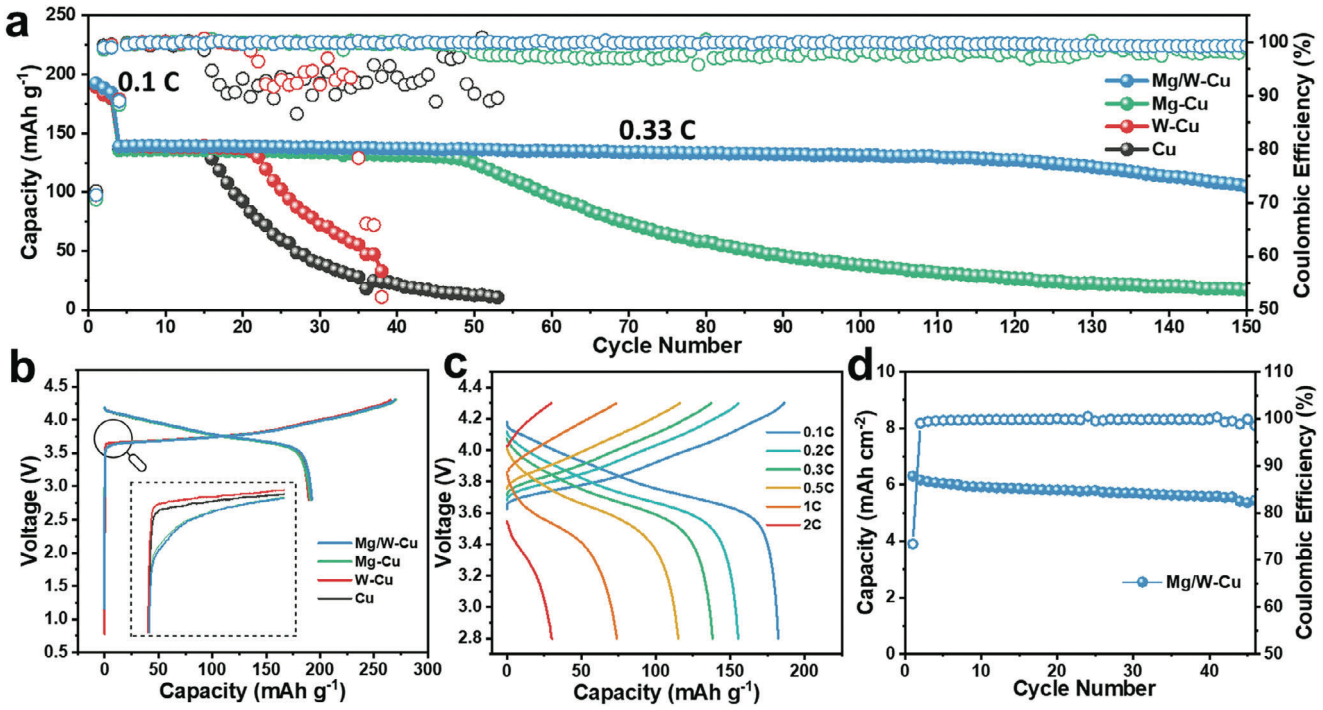

Figure 6. a) Cycling performance of NMC full cells, tested at 0.33C after initial 3 cycles at 0.1C. b) Galvanostatic profiles at 1st cycle at 0.1C. c) Rate capability of Mg/W-Cu|SE|NMC cell. d) Cycling performance of Mg/W-Cu|SE|NMC cell with high NMC mass-loading at 0.2C.

significant volume expansion, causing delamination of the Sn coating from the Cu current collector and reducing its effectiveness in preventing Cu corrosion.

The diffusion mechanism of Li on the surface of W was investigated using nudged elastic band (NEB) and adaptive kinetic Monte Carlo (aKMC) calculations to determine the diffusion energy barriers of Li atoms within the W bulk region and on the surface of W layer. The free energy diagram and schematic illustration of specific diffusion pathways for a single Li atom in the bulk and on the surfaces of W are shown in Figure S30 in the Supporting Information. As summarized in Table S3 (Supporting Information), the diffusion barrier of a single Li atom within the W bulk (0.28 eV) is higher than that on the W (110) surface (0.1 eV). This indicates that Li atoms preferentially remain on the surface rather than diffusing into the bulk region and the W underlayer remains truly inactive towards Li ions, avoiding any alloying effects beyond the minimal thermodynamically – dictated solubility. Due to analogous phase diagrams with Li (negligible room temperature solubility, no intermediate phases), one would expect similar findings for diffusivity of Li on/in refractory Mo and Nb layers. Such behavior is distinct from the well-studied Li-active metals such as Mg, Sn, Ag, Au, and Sb. These metals possess significant solubility with Li, which may be reversed at every electrodissolution cycle depending on the rate and the cut-off voltage. It is also distinct from lithiophilic intermetallics such as Li_2Te, which contain stoichiometric amounts of lithium in their equilibrium structure, but that cannot be extracted at anode-relevant voltages.[34] Combining an alloying film facing the SE with an inert protective film facing the Cu collector therefore appears to be optimum for tuning electrodeposition/dissolution while minimizing corrosion.

As proof of concept, AF-ASSBs were fabricated and tested using Mg/W-Cu, Mg-Cu, W-Cu, and baseline Cu current collectors. With AF-ASSBs, it is necessary to achieve cycling CEs approaching 100% since there is no secondary Li reservoir apart from the Li stored in the cathode. The anode-free full cells were assembled using a composite cathode consisting of commercial $LiNbO_3$-coated $LiNi_{0.8}Mn_{0.1}Co_{0.1}O_2$ (LNO@NMC811) and LPSCl, at a weight ratio of 7:3 without any carbon additives. The areal capacity of cathode is ≈1 mAh cm^{-2} for "standard" tests and over 8 mAh cm^{-2} for "high mass-loading" experiments. The CEs in the AF-ASSBs are calculated based on the discharge and charge capacities of the composite cathodes. **Figure 6a** compares the long-term cycling performance of the Mg/W-Cu, Mg-Cu, W-Cu, and baseline Cu AF-ASSBs. All cells were activated at 0.1C (1C equals 200 mA g^{-1} based on the mass of NMC cathode) for 3 cycles before switching to 0.33C. The electrochemical measurements were carried out within the voltage window of 2.8–4.3 V at room temperature.

Figure 6b provides the galvanostatic profiles of the cells for the 0.1C activation. The AF-ASSBs employing Mg/W-Cu, Mg-Cu, W-Cu, and baseline Cu current collectors exhibit charge/discharge capacities of 269/192 mAh g^{-1}, 270/191 mAh g^{-1}, 265/189 mAh g^{-1}, and 265/192 mAh g^{-1}, resulting in approximate initial Coulombic efficiencies (ICEs) of 71%, 71%, 71%, and 72%, respectively. The inset in Figure 6b shows an enlarged view at the beginning of charge process, revealing a marked difference in the voltage profiles among these samples. Figure S31 (Supporting Information) presents the galvanostatic profiles of these cells starting from the 5th and 10th cycles, followed by every 10 cycles until 150th cycle or cell failure. W-Cu and Cu full cells exhibit higher initial charging voltages compared to Mg/W-Cu and

Mg-Cu cells, with minimal differences in the subsequent voltage profiles. The elevated overpotential for electrodeposition on both W-Cu and baseline Cu collectors reduces the effective voltage available at the cathode. In standard tests, a mass loading of approximately 1 mAh cm^{-2} was used, with a 0.1C rate corresponding to an areal current density of ≈0.1 mAh cm^{-2}. Figure S32 (Supporting Information) presents cycle 1 galvanostatic electrodeposition profiles for half-cells using Mg/W-Cu, Mg-Cu, W-Cu, and baseline Cu current collectors at a 0.1C rate. These results demonstrate that Mg/W-Cu and Mg-Cu current collectors exhibit a notably lower early-stage overpotential than do the W-Cu and baseline Cu collectors. A lower early-stage electrodeposition overpotential translates into less voltage needed during the early stage charging of an anode-free full cell, where Li ions are first extracted from the cathode and electrodeposited onto the current collector. This explains the trend presented in the inset of Figure 6b.

After switching to a higher current of 0.33C, the cells initially display a comparable discharge capacity, in the range of 135–139 mAh g^{-1}. However, Cu|SE|NMC and W-Cu|SE|NMC cells experience rapid capacity decay after 15 and 21 cycles, respectively. The Mg-Cu|SE|NMC cell shows extended cycle life up to 50 cycles when the capacity begins to decline. In contrast, the Mg/W-Cu|SE|NMC cell did not show any significant capacity loss within 120 cycles, sustaining a specific capacity of 122 mAh g^{-1}. This corresponds to a capacity decay rate of 0.06% per cycle. Afterwards, a gradual capacity decrease is observed with a faster decay rate of 0.58% per cycle from cycle 130–150. Overall, the Mg/W-Cu|SE|NMC AF-ASSB delivers a capacity retention of 76% after 150 cycles at 0.33C. Such electrochemical performance is among the most favorable, per Table S4, Supporting Information.

It should also be noted that the cycling performance of anode-free full cells is not directly comparable to that of half-cells. With anode-free full cells the available Li ion reservoir is limited by what is initially stored in the cathode, all Li losses lead to corresponding CE and capacity decay. With half-cells, their relatively thick Li foils serve as a near infinite reservoir of capacity. For example, a 100 µm Li foil corresponds to 20 mAh cm^{-2}, far above the 3–4 mAh cm^{-2} of commercially relevant cells. During cycling when Li is lost to the SEI, dead metal, etc. the CE decays but the available capacity does not. Therefore to simulate the half-cell configuration in an anode-free cell, a limited-capacity charge protocol was applied. Specifically, the Mg/W-Cu|SE|NMC AF-ASSB underwent an initial activation cycle at 0.1C for three cycles within a potential window of 2.8–4.3 V. Subsequently, the cell was charged to 50% of its capacity (50% depth-of-charge, DOC) and discharged to 2.8 V at a current density of 0.33C. This left 50% of Li in the cathode as a reservoir to compensate for Li loss during cycling.

Figure S33a (Supporting Information) shows the cycling performance of the Mg/W-Cu|SE|NMC cell under 50% DOC and Figure S33b (Supporting Information) presents the galvanostatic cycling profiles over the initial 10 cycles. The cell exhibits charge/discharge capacities of 285/203 mAh g^{-1} and 199/197 mAh g^{-1} in the first two cycles, corresponding to CEs of 71% and 99%, respectively. Upon switching to 0.33C, the charge capacity was set to 100 mAh g^{-1}, which is ≈50% of the total cell capacity. The initial cycle at 0.33C delivers a discharge capacity of 84 mAh g^{-1}, with a CE of 84%. Subsequent cycles yield stable discharge capacities of 100 ± 0.5 mAh g^{-1} with an average cycling CE of 99.96% for up to 256 cycles. These results indicate that comparable cycling stability can be achieved in AF-ASSB with an additional Li reservoir in the cathode, consistent with the electrochemical measurements observed in half-cells.

Figures 6c and S34 (Supporting Information) display the rate capability of the Mg/W-Cu|SE|NMC cell, with discharge capacities of 183, 155, 138, 115, 74, and 30 being obtained at 0.1C, 0.2C, 0.3C, 0.5C, 1C, and 2C, respectively. Figure S35 (Supporting Information) provides the cycling stability at a higher current density of 0.5C. A reversible capacity of 115 mAh g^{-1} can be obtained after 150 cycles with a capacity decay rate of 0.03% per cycle. In order to test the practicality of the Mg/W-Cu|SE|NMC cell, a high mass-loading NMC cathode was employed with an areal capacity exceeding 8 mAh cm^{-2}, almost twice as much as commercial lithium-ion batteries cathode (4 mAh cm^{-2}). As shown in Figure 6d, the high mass-loading Mg/W-Cu|SE|NMC cell delivered an initial charge and discharge capacities of 8.6 and 6.3 mAh cm^{-2} at 0.2C, corresponding to an ICE of 73.4%. The cell stably cycled for more than 45 cycles, exhibiting a capacity retention of 86.5%. It is noteworthy that with such a high areal capacity, a thickness of more than 30 µm Li is being electrodeposited and electrodissolved for each cycle.

3. Conclusions

Conventional thinking regarding electrochemical stability of battery anodes considers a single solid electrolyte interphase (SEI). However, here it is demonstrated that electrochemical stability of an anode-free all solid-state battery (AF-ASSB) employing argyrodite solid electrolyte requires the following interrelated attributes: Lithium has to uniformly electrodeposit/dissolve onto/from both the "empty" Cu current collector and the pre-existing Li metal. In parallel, the Li-SE and Cu-SE interphases (SEI-1 and SEI-2) have to remain stable and minimally corroded. To date SEI-2 and its contribution to ultimate cell failure has been largely overlooked. Microstructural control of these complex interfaces and interphases is achieved with physical vapor deposited (PVD, magnetron sputtering) bilayer of 140 nm Mg / 30 nm W onto the collector surface (Mg/W-Cu). Through detailed analytical work, including cryo-FIB microscopy, the following phenomenology is identified: The Mg collector coating promotes uniform Li metal electrodeposition/dissolution onto/from the current collector through reversible alloying, in-turn stabilizing the solid electrolyte interphase (SEI-1). The refractory W underlayer prevents irreversible corrosion of the collector by the SE to form copper sulfides (SEI-2); Dedicated corrosion experiments demonstrate that Mg itself cannot prevent parasitic formation of copper sulfide, explaining why such single alloy layer historically provide limited efficacy. Mesoscale modeling demonstrates that the shear stress between the thickening *bcc* Li_xMg alloy and the SE (they are mechanically coupled through the SEI) promotes Li segregation away from that interface. These findings provide a new design paradigm necessary for anode-free (AF) systems, since contact between the collector and the SE is unavoidable at full discharge.

4. Experimental Section

Materials Preparation: Fabrication of modified current collectors—The current collectors, composed of Mg/W-Cu, Mg/Mo-Cu, Mg/Nb-Cu, Mg/Sn-Cu, Mg-Cu, and W-Cu were fabricated utilizing the physical vapor deposition (PVD) technique employing the 'Orion-8" sputtering system by AJA Instruments. The deposition occurred within a turbo-pumped chamber, which was evacuated to a base pressure of less than 10^{-8} torr before commencement of any deposition process. The deposition utilized pure Mg (2.0" diameter, 0.25" thickness, 99.95% purity), W (2.0" diameter, 0.25" thickness, 99.95% purity), Mo (2.0" diameter, 0.25" thickness, 99.95% purity), Nb (2.0" diameter, 0.25" thickness, 99.95% purity), and Sn (2.0" diameter, 0.125" thickness, 99.95% purity) as targets, both sourced from AJA Instruments. Radio frequency (RF) magnetron sputtering mode was uniformly employed for all deposition processes. The target guns were connected to a water-cooled chiller, with ultrapure Argon serving as the carrier gas. Precise control of Argon gas flow rates, achieved through gas flowmeter, was maintained at a standardized rate of 32 SCCM (SCCM denoting standard cubic centimeters per minute) for all depositions. A battery-grade square shaped copper sheet (5 cm × 5 cm, 9 µm thickness, MTI Corporation, USA), was affixed to the rotating substrate holder of the instrumentation. This holder was mounted at a distance of 22 cm from the target. The gun energy was set to be 100 kWh for Sn, 150 kWh for Mg, and 200 kWh for W, Mo, and Nb. The film deposition rate was calibrated using quartz crystals monitor.

Li_6PS_5Cl solid-electrolyte—Commercial argyrodite Li_6PS_5Cl SE was purchased from NEI Corporation, USA. To prepare wet ball milled SE, four grams of LPSCl SE was added to a 50 mL zirconia milling jar containing 20 zirconia milling balls (6 mm diameter). Then, 4.8 mL anhydrous m-xylene was added, and the milling jar was vacuum-sealed inside the glovebox. Wet ball milling was conducted on a planetary ball mill machine (PM100, Retsch) at a speed of 300 rpm for 24 h with 5 min rest for every 20 min milling to allow heat dissipation. Finally, the electrolyte was obtained after drying in the glove box at 80 °C overnight. The XRD profiles in shown in Figure S36a (Supporting Information) and the ionic conductivity at room temperature is calculated to be 0.8 mS cm^{-1} under a pressure of 9 MPa, per Figure S36b in the Supporting Information.

Cell Assembly: All-solid-state half-cells cells—150 mg milled LPSCl SE powder was first pressed using a hydraulic press (YLJ-24TS, MTI Corporation, USA) under 50 MPa in a polyether ether ketone (PEEK) mold (12 mm in diameter). Then, a piece of current collector (Mg/W-Cu or Mg-Cu or W-Cu or Cu) foil (12 mm in diameter) was attached to one side of the pellet and subsequently pressed at 530 MPa for 1 min. Next, a piece of Li chip was sandwiched in a plastic bakery bag and rolled to a thickness of around 100 µm, and a piece of 8 mm diameter Li foil was attached to the other side of the pellet without compressing. Afterwards, the cell was positioned in the cell case and tightened using a torque wrench. A torque of 20 lb in (corresponding to 9 MPa pressure) was employed, the pressure being measured using torque wrench with additional torque-pressure calibration being performed at Oak Ridge National Laboratory.

Anode-free all-solid-state batteries (AF-ASSBs)—The composite cathode was prepared by hand mixing $LiNbO_3$-coated NMC811 cathode (NEI Corporation, USA) with SE powder at a weight ratio of 7:3 in a mortar for 40 min. When assembling the battery, 150 mg milled LPSCl SE powder was first pressed under 50 MPa in PEEK mold. Then the composite cathode powder was uniformly dispersed on one side of the SE pellet and a piece of current collector (Mg/W-Cu or Mg-Cu or W-Cu or Cu) foil was placed on the other side. The areal capacity of cathode is ≈1 mAh cm^{-2} for typical measurements and ≈8 mAh cm^{-2} for high mass-loading experiments. The entire cell was further pressed under 867 MPa for 2 min and finally positioned in the cell housing tightened to 30 lb in with a torque wrench. The stack pressure is measured to be ≈14 MPa.

Electrochemical Measurements: Galvanostatic cycling was conducted on Land CT2001A battery testers. The current densities and capacities employed during testing are noted in the descriptions of the analyses and the captions of the associated figures. Electrochemical impedance spectroscopy (EIS) tests were recorded on a Princeton PARSTAT MC electrochemical workstation in the frequency range of 1 MHz – 1 Hz with an amplitude of 10 mV. The obtained data was analyzed using the Z-View software. Ionic conductivity of SEs was calculated based on the equation of $\sigma = L/(R_b A)$, where L is the thickness of the electrolyte pellet, R_b is the bulk resistance of SE, and A is the area of the SE layer. All electrochemical measurements in this work were carried out at room temperature (≈23 °C).

Material Characterization: Room-temperature and cryogenic scanning electron microscopy (SEM) and focused-ion beam (FIB) SEM were both performed on a Thermo Scientific Scios 2 Dual Beam SEM/FIB with a Leica VCT cryogenic stage and energy dispersive X-ray spectrometer (EDXS). To preserve the structural integrity of the beam-sensitive Li-based materials and to reduce artificial inclusion, the sample was cooled to −150 °C. The Ga^+ FIB milling was performed at an accelerating voltage of 30 keV with currents ranging from 1 to 50 nA. X-ray diffraction (XRD) profiles were recorded on Rigaku Miniflex 600 diffractometer with Cu Kα radiation (λ = 1.54178 Å) at a scan rate of 5° per minute within the 2θ range from 10° to 80°. X-ray photoelectron spectroscopy (XPS) analyses were performed using a Kratos Axis Ultra DLD XPS (manufactured by Kratos Analytical, Inc.), equipped with an Al Kα monochromatic X-ray source with a power set at 120 W. The photoelectrons were collected with an emission angle (EA) of 90° and from a sample area of 300 µm × 700 µm. For high-resolution spectra, the measurements were performed in constant-analyzer-energy (CAE) mode with a pass energy of 20 eV and a step size of 0.1 eV (full-width-at-half-maximum of the peak for Ag $3d_{5/2}$ is 0.77 eV). The residual pressure in the analytical chamber was ≈5 × 10^{-9} Torr. Depth profiling analysis of the samples was performed by time-of-flight secondary ion mass spectrometry (TOF-SIMS) on an M6 TOF-SIMS instrument produced by ionTOF GmbH (Germany, 2023). During depth profiling, a Bi^+ analysis ion beam (30 keV ion energy, ≈0.5 pA measured sample current), raster scanning 100 µm × 100 µm areas, was used to produce secondary ions that were further detected through a time-of-flight analyzer, while an O^{2+} sputtering ion beam (1 keV ion energy, ≈41 nA measured sample current) was used to ablate the surface in 300 µm × 300 µm areas centered around the Bi^+ analysis areas. All detected ions had positive polarity, with an ultrahigh mass resolution better than 15 000 (m/dm). The measurements were performed in an ultrahigh vacuum at a base pressure of ≈10^{-10} mbar. Nanoindentation was performed using a Hysitron TI 950 TriboIndenter. Reduced modulus was calculated using Hysitron software by fitting the unloading force–displacement curve using the Berkovich probe (TI-0039) tip area calibration and the Oliver and Pharr method. All samples were indented in triplicate for each load function. The load function consisted of loading the sample to a maximum displacement of 500 nm over a 10 s period, kept at that displacement for 10 s, and then unloaded over a 3 s period. All postcycled electrodes were extracted from disassembled cells in an Ar-filled glovebox (<0.1 ppm of H_2O and O_2).

Supporting Information

Supporting Information is available from the Wiley Online Library or from the author.

Acknowledgements

Y.W. and D.M. were supported by the Assistant Secretary for Energy Efficiency and Renewable Energy, Office of Vehicle Technologies of the U.S. Department of Energy (DOE) through the Advanced Battery Materials Research Program (Battery500 Consortium). V.R., K.G.N., B.S.V., and P.P.M. were supported by the Mechano-Chemical Understanding of Solid Ion Conductors, an Energy Frontier Research Center funded by the U.S. Department of Energy, Office of Science, Office of Basic Energy Science, contact DE-SC0023438. E.A.R. and Z.A.P. were supported by The Welch Foundation under Grant No. F-2007 (nanoindentation characterization) and E.A.R. was supported by the National Science Foundation (NSF) Division of Graduate Education (DGE) through the Graduate Research Fellowship Program under Grant No. 2137420. The acquisition of XPS was supported by the National Science Foundation Major Research Instrumentation program (Grant No. 2117623). This work was performed, in part, at

the Center for Integrated Nanotechnologies, an Office of Science User Facility operated by the U.S. Department of Energy (DOE) Office of Science. Los Alamos National Laboratory, an affirmative action equal opportunity employer, is managed by Triad National Security, LLC for the U.S. Department of Energy's NNSA, under contract 89233218CNA000001. J.C., M.N., and G.H. were supported by Texas Advanced Computing Center (TACC) and Advanced Cyberinfrastructure Coordination Ecosystem: Services and Support (ACCESS) – CHE190010. This work was supported by The Welch Foundation (F-2206).

Conflict of Interest

The authors declare no conflict of interest.

Data Availability Statement

The data that support the findings of this study are available from the corresponding author upon reasonable request.

Keywords

all-solid-state battery (ASSB), anode-free battery, cryogenic microscopy, solid-state electrolyte (SE), sulfide electrolyte

Received: July 26, 2024
Revised: October 6, 2024
Published online: January 6, 2025

[1] J. B. Goodenough, Y. Kim, *Chem. Mater.* **2009**, *22*, 587.
[2] Y. Zhu, J. C. Gonzalez-Rosillo, M. Balaish, Z. D. Hood, K. J. Kim, J. L. M. Rupp, *Nat. Rev. Mater.* **2020**, *6*, 313.
[3] D. H. S. Tan, A. Banerjee, Z. Chen, Y. S. Meng, *Nat. Nanotechnol.* **2020**, *15*, 170.
[4] J. Janek, W. G. Zeier, *Nat. Energy* **2016**, *1*, 16141.
[5] P. Albertus, V. Anandan, C. Ban, N. Balsara, I. Belharouak, J. Buettner-Garrett, Z. Chen, C. Daniel, M. Doeff, N. J. Dudney, B. Dunn, S. J. Harris, S. Herle, E. Herbert, S. Kalnaus, J. A. Libera, D. Lu, S. Martin, B. D. McCloskey, M. T. McDowell, Y. S. Meng, J. Nanda, J. Sakamoto, E. C. Self, S. Tepavcevic, E. Wachsman, C. Wang, A. S. Westover, J. Xiao, T. Yersak, *ACS Energy Lett.* **2021**, *4*, 1399.
[6] V. Raj, V. Venturi, V. R. Kankanallu, B. Kuiri, V. Viswanathan, N. P. B. Aetukuri, *Nat. Mater.* **2022**, *21*, 1050.
[7] R. Pacios, A. Villaverde, M. Martínez-Ibañez, M. Casas-Cabanas, F. Aguesse, A. Kvasha, *Adv. Energy Mater.* **2023**, *13*, 2301018.
[8] C. Wang, J. Liang, J. T. Kim, X. Sun, *Sci. Adv.* **2022**, *8*, adc9516.
[9] C. X. Bi, M. Zhao, L. P. Hou, Z. X. Chen, X. Q. Zhang, B. Q. Li, H. Yuan, J. Q. Huang, *Adv. Sci.* **2022**, *9*, 2103910.
[10] S. Kim, G. Park, S. J. Lee, S. Seo, K. Ryu, C. H. Kim, J. W. Choi, *Adv. Mater.* **2023**, *35*, 2206625.
[11] J. Liu, Z. Bao, Y. Cui, E. J. Dufek, J. B. Goodenough, P. Khalifah, Q. Li, B. Y. Liaw, P. Liu, A. Manthiram, Y. S. Meng, V. R. Subramanian, M. F. Toney, V. V. Viswanathan, M. S. Whittingham, J. Xiao, W. Xu, J. Yang, X.-Q. Yang, J.-G. Zhang, *Nat. Energy* **2019**, *4*, 180.
[12] P. Shi, X. Q. Zhang, X. Shen, R. Zhang, H. Liu, Q. Zhang, *Adv. Mater. Technol.* **2020**, *5*, 1900806.
[13] J. Kang, D. Y. Han, S. Kim, J. Ryu, S. Park, *Adv. Mater.* **2023**, *35*, 2203194.
[14] V. Raj, N. P. B. Aetukuri, J. Nanda, *Curr. Opin. Solid State Mater. Sci.* **2022**, *26*, 100999.
[15] H. Zhao, W. Y. A. Lam, L. Sheng, L. Wang, P. Bai, Y. Yang, D. Ren, H. Xu, X. He, *Adv. Energy Mater.* **2022**, *12*, 2103894.
[16] X. Feng, H. Fang, N. Wu, P. Liu, P. Jena, J. Nanda, D. Mitlin, *Joule* **2022**, *6*, 543.
[17] Q. Lv, Y. Jiang, B. Wang, Y. Chen, F. Jin, B. Wu, H. Ren, N. Zhang, R. Xu, Y. Li, T. Zhang, Y. Zhou, D. Wang, H. Liu, S. Dou, *Cell Rep. Phys. Sci.* **2022**, *3*, 100706.
[18] C. Wang, C. Wang, M. Li, S. Zhang, C. Zhang, S. Chou, J. Mao, Z. Guo, *Mater. Today* **2023**, *72*, 235.
[19] J. Gu, H. Zhong, Z. Chen, J. Shi, Z. Gong, Y. Yang, *Chem. Eng. J.* **2023**, *454*, 139923.
[20] H. Liu, Y. Liang, C. Wang, D. Li, X. Yan, C. W. Nan, L. Z. Fan, *Adv. Mater.* **2023**, *35*, 2206013.
[21] J. Wang, L. Chen, H. Li, F. Wu, *Energy Environ. Mater.* **2023**, *6*, 12613.
[22] J. Kasemchainan, S. Zekoll, D. S. Jolly, Z. Ning, G. O. Hartley, J. Marrow, P. G. Bruce, *Nat. Mater.* **2019**, *18*, 1105.
[23] S. Randau, D. A. Weber, O. Kötz, R. Koerver, P. Braun, A. Weber, E. Ivers-Tiffée, T. Adermann, J. Kulisch, W. G. Zeier, F. H. Richter, J. Janek, *Nat. Energy* **2020**, *5*, 259.
[24] J. Zhang, C. Zheng, L. J. Li, Y. Xia, H. Huang, Y. P. Gan, C. Liang, X. P. He, X. Y. Tao, W. K. Zhang, *Adv. Energy Mater.* **2020**, *10*, 1903311.
[25] Q. Zhang, D. Cao, Y. Ma, A. Natan, P. Aurora, H. Zhu, *Adv. Mater.* **2019**, *31*, 1901131.
[26] D. H. S. Tan, E. A. Wu, H. Nguyen, Z. Chen, M. A. T. Marple, J. M. Doux, X. F. Wang, H. D. Yang, A. Banerjee, Y. S. Meng, *ACS Energy Lett.* **2019**, *4*, 2418.
[27] S. Narayanan, U. Ulissi, J. S. Gibson, Y. A. Chart, R. S. Weatherup, M. Pasta, *Nat. Commun.* **2022**, *13*, 7237.
[28] A. Banerjee, X. Wang, C. Fang, E. A. Wu, Y. S. Meng, *Chem. Rev.* **2020**, *120*, 6878.
[29] S. Li, S. J. Yang, G. X. Liu, J. K. Hu, Y. L. Liao, X. L. Wang, R. Wen, H. Yuan, J. Q. Huang, Q. Zhang, *Adv. Mater.* **2023**, *36*, 2307768.
[30] F. Ren, Z. Liang, W. Zhao, W. Zuo, M. Lin, Y. Wu, X. Yang, Z. Gong, Y. Yang, *Energy Environ. Sci.* **2023**, *16*, 2579.
[31] D. Zeng, J. Yao, L. Zhang, R. Xu, S. Wang, X. Yan, C. Yu, L. Wang, *Nat. Commun.* **2022**, *13*, 1909.
[32] H. Hao, Y. Liu, S. M. Greene, G. Yang, K. G. Naik, B. S. Vishnugopi, Y. Wang, H. Celio, A. Dolocan, W. Y. Tsai, R. Fang, J. Watt, P. P. Mukherjee, D. J. Siegel, D. Mitlin, *Adv. Energy Mater.* **2023**, *13*, 2301338.
[33] Y. Wang, H. Hao, K. G. Naik, B. S. Vishnugopi, C. D. Fincher, Q. Yan, V. Raj, H. Celio, G. Yang, H. Fang, Y. M. Chiang, F. A. Perras, P. Jena, J. Watt, P. P. Mukherjee, D. Mitlin, *Adv. Energy Mater.* **2024**, *14*, 2304530.
[34] Y. Wang, Y. Liu, M. Nguyen, J. Cho, N. Katyal, B. S. Vishnugopi, H. Hao, R. Fang, N. Wu, P. Liu, P. P. Mukherjee, J. Nanda, G. Henkelman, J. Watt, D. Mitlin, *Adv. Mater.* **2023**, *35*, 2206762.
[35] M. Li, B. Wang, J. Ma, Z. Wang, Y. Liang, Z. Wang, L. Zhang, Y. Tang, Q. Huang, J. Huang, *Adv. Energy Mater.* **2023**, *14*, 2303156.
[36] B. S. Vishnugopi, E. Kazyak, J. A. Lewis, J. Nanda, M. T. McDowell, N. P. Dasgupta, P. P. Mukherjee, *ACS Energy Lett.* **2021**, *6*, 3734.
[37] J. M. Doux, H. Nguyen, D. H. S. Tan, A. Banerjee, X. Wang, E. A. Wu, C. Jo, H. Yang, Y. S. Meng, *Adv. Energy Mater.* **2019**, *10*, 1903253.
[38] J. A. Lewis, F. J. Q. Cortes, Y. Liu, J. C. Miers, A. Verma, B. S. Vishnugopi, J. Tippens, D. Prakash, T. S. Marchese, S. Y. Han, C. Lee, P. P. Shetty, H. W. Lee, P. Shevchenko, F. De Carlo, C. Saldana, P. P. Mukherjee, M. T. McDowell, *Nat. Mater.* **2021**, *20*, 503.
[39] B. S. Vishnugopi, K. G. Naik, H. Kawakami, N. Ikeda, Y. Mizuno, R. Iwamura, T. Kotaka, K. Aotani, Y. Tabuchi, P. P. Mukherjee, *Adv. Energy Mater.* **2022**, *13*, 2203671.
[40] T. Krauskopf, F. H. Richter, W. G. Zeier, J. Janek, *Chem. Rev.* **2020**, *120*, 7745.
[41] T. Krauskopf, H. Hartmann, W. G. Zeier, J. Janek, *ACS Appl. Mater. Interfaces* **2019**, *11*, 14463.
[42] L. Song, R. Li, H. Zhu, Z. Li, G. Liu, Z. Peng, X. Fan, X. Yao, *Adv. Mater.* **2024**, *36*, 2400165.

[43] R. Weber, M. Genovese, A. J. Louli, S. Hames, C. Martin, I. G. Hill, J. R. Dahn, *Nat. Energy* **2019**, *4*, 683.
[44] M. Genovese, A. J. Louli, R. Weber, S. Hames, J. R. Dahn, *J. Electrochem. Soc.* **2018**, *165*, A3321.
[45] S. Chen, J. Zhang, L. Nie, X. Hu, Y. Huang, Y. Yu, W. Liu, *Adv. Mater.* **2021**, *33*, 2002325.
[46] C. Heubner, S. Maletti, H. Auer, J. Hüttl, K. Voigt, O. Lohrberg, K. Nikolowski, M. Partsch, A. Michaelis, *Adv. Funct. Mater.* **2021**, *31*, 2106608.
[47] W. Z. Huang, C. Z. Zhao, P. Wu, H. Yuan, W. E. Feng, Z. Y. Liu, Y. Lu, S. Sun, Z. H. Fu, J. K. Hu, S. J. Yang, J. Q. Huang, Q. Zhang, *Adv. Energy Mater.* **2022**, *12*, 2201044.
[48] J. Wen, T. Wang, C. Wang, Y. Dai, Z. Song, X. Liu, Q. Yu, X. Zheng, J. Ma, W. Luo, Y. Huang, *Adv. Mater.* **2023**, *36*, 2307732.
[49] Y. Wang, H. Dong, N. Katyal, H. Hao, P. Liu, H. Celio, G. Henkelman, J. Watt, D. Mitlin, *Adv. Mater.* **2022**, *34*, 2106005.
[50] B. Neudecker, N. Dudney, J. Bates, *J. Electrochem. Soc.* **2000**, *147*, 517.
[51] A. S. Westover, R. L. Sacci, N. Dudney, *ACS Energy Lett.* **2020**, *5*, 3860.
[52] D. Cheng, R. Shimizu, J. Weaver, Y. S. Meng, *Microsc. Microanal.* **2021**, *27*, 3324.
[53] M. J. Wang, E. Carmona, A. Gupta, P. Albertus, J. Sakamoto, *Nat. Commun.* **2020**, *11*, 5201.
[54] Y.-G. Lee, S. Fujiki, C. Jung, N. Suzuki, N. Yashiro, R. Omoda, D.-S. Ko, T. Shiratsuchi, T. Sugimoto, S. Ryu, J. H. Ku, T. Watanabe, Y. Park, Y. Aihara, D. Im, I. T. Han, *Nat. Energy* **2020**, *5*, 299.
[55] C. Wang, S. Hwang, M. Jiang, J. Liang, Y. Sun, K. Adair, M. Zheng, S. Mukherjee, X. Li, R. Li, H. Huang, S. Zhao, L. Zhang, S. Lu, J. Wang, C. V. Singh, D. Su, X. Sun, *Adv. Energy Mater.* **2021**, *11*, 2100210.
[56] J. Zhou, M. L. Holekevi Chandrappa, S. Tan, S. Wang, C. Wu, H. Nguyen, C. Wang, H. Liu, S. Yu, Q. R. S. Miller, G. Hyun, J. Holoubek, J. Hong, Y. Xiao, C. Soulen, Z. Fan, E. E. Fullerton, C. J. Brooks, C. Wang, R. J. Clement, Y. Yao, E. Hu, S. P. Ong, P. Liu, *Nature* **2024**, *627*, 301.
[57] R. Guo, K. Zhang, W. Zhao, Z. Hu, S. Li, Y. Zhong, R. Yang, X. Wang, J. Wang, C. Wu, Y. Bai, *Energy Mater. Adv.* **2023**, *4*, 0022.
[58] H. Wan, Z. Wang, W. Zhang, X. He, C. Wang, *Nature* **2023**, *623*, 739.
[59] X. Miao, S. Guan, C. Ma, L. Li, C. W. Nan, *Adv. Mater.* **2023**, *35*, 2206402.
[60] L. Hu, Y. Ren, C. Wang, J. Li, Z. Wang, F. Sun, J. Ju, J. Ma, P. Han, S. Dong, G. Cui, *Adv. Mater.* **2024**, *36*, 2401909.
[61] K. G. Naik, B. S. Vishnugopi, J. Datta, D. Datta, P. P. Mukherjee, *Appl. Mech. Rev.* **2023**, *75*, 010802.
[62] J. C. Vickerman, *ToF-SIMS: Surface Analysis by Mass Spectrometry* **2001**, 1.
[63] D. H. Tan, Y.-T. Chen, H. Yang, W. Bao, B. Sreenarayanan, J.-M. Doux, W. Li, B. Lu, S.-Y. Ham, B. Sayahpour, *Science* **2021**, *373*, 1494.
[64] L. Ye, X. Li, *Nature* **2021**, *593*, 218.
[65] J. Y. Kim, S. Jung, S. H. Kang, J. Park, M. J. Lee, D. Jin, D. O. Shin, Y. G. Lee, Y. M. Lee, *Adv. Energy Mater.* **2021**, *12*, 2103108.
[66] K. Yan, Z. Lu, H.-W. Lee, F. Xiong, P.-C. Hsu, Y. Li, J. Zhao, S. Chu, Y. Cui, *Nat. Energy* **2016**, *1*, 16010.
[67] A. Kohandehghan, P. Kalisvaart, M. Kupsta, B. Zahiri, B. S. Amirkhiz, Z. Li, E. L. Memarzadeh, L. A. Bendersky, D. Mitlin, *J. Mater. Chem. A* **2013**, *1*, 1600.
[68] C. Yang, H. Xie, W. Ping, K. Fu, B. Liu, J. Rao, J. Dai, C. Wang, G. Pastel, L. Hu, *Adv. Mater.* **2019**, *31*, 1804815.
[69] P. Gao, H. Wu, X. Zhang, H. Jia, J. M. Kim, M. H. Engelhard, C. Niu, Z. Xu, J. G. Zhang, W. Xu, *Angew. Chem., Int. Ed.* **2021**, *60*, 16506.
[70] S. Kaboli, P. Noel, D. Clément, H. Demers, A. Paolella, P. Bouchard, M. L. Trudeau, J. B. Goodenough, K. Zaghib, *Sci. Adv.* **2020**, *6*, abd5708.
[71] L. Zhao, W. Li, C. Wu, Q. Ai, L. Guo, Z. Chen, J. Zheng, M. Anderson, H. Guo, J. Lou, Y. Liang, Z. Fan, J. Zhu, Y. Yao, *Adv. Energy Mater.* **2023**, *13*, 2300679.
[72] L. Beaulieu, K. Eberman, R. Turner, L. Krause, J. Dahn, *Electrochem. Solid-State Lett.* **2001**, *4*, A137.
[73] B. D. Adams, J. Zheng, X. Ren, W. Xu, J. G. Zhang, *Adv. Energy Mater.* **2017**, *8*, 1702097.
[74] Z. Wang, J. Xia, X. Ji, Y. Liu, J. Zhang, X. He, W. Zhang, H. Wan, C. Wang, *Nat. Energy* **2024**, *9*, 251.
[75] C. Wang, T. Deng, X. Fan, M. Zheng, R. Yu, Q. Lu, H. Duan, H. Huang, C. Wang, X. Sun, *Joule* **2022**, *6*, 1770.
[76] M. J. Counihan, K. S. Chavan, P. Barai, D. J. Powers, Y. Zhang, V. Srinivasan, S. Tepavcevic, *Joule* **2024**, *8*, 64.
[77] M. Siniscalchi, J. Liu, J. S. Gibson, S. J. Turrell, J. Aspinall, R. S. Weatherup, M. Pasta, S. C. Speller, C. R. M. Grovenor, *ACS Energy Lett.* **2022**, *7*, 3593.
[78] T. Krauskopf, B. Mogwitz, C. Rosenbach, W. G. Zeier, J. Janek, *Adv. Energy Mater.* **2019**, *9*, 1902568.
[79] Y. Zhang, K. S. R. Chandran, M. Jagannathan, H. Z. Bilheux, J. C. Bilheux, *J. Electrochem. Soc.* **2017**, *164*, A28.
[80] P. Balaya, J. Maier, *Phys. Chem. Chem. Phys.* **2010**, *12*, 215.
[81] J.-S. Kim, G. Yoon, S. Kim, S. Sugata, N. Yashiro, S. Suzuki, M.-J. Lee, R. Kim, M. Badding, Z. Song, *Nat. Commun.* **2023**, *14*, 782.
[82] F. Xie, M. S. Diallo, H. Kim, Q. H. Tu, G. Ceder, *Adv. Energy Mater.* **2024**, *14*, 2302960.
[83] H. Okamoto, M. E. Schlesinger, E. M. Mueller, *Alloy Phase Diagrams*, Vol. *3*, ASM International **2016**.
[84] R. Guo, L. Lu, M. Ouyang, X. Feng, *Sci. Rep.* **2016**, *6*, 30248.
[85] L. Guo, D. B. Thornton, M. A. Koronfel, I. E. L. Stephens, M. P. Ryan, *J. Phys. Energy* **2021**, *3*, 032015.
[86] A. Jain, S. P. Ong, G. Hautier, W. Chen, W. D. Richards, S. Dacek, S. Cholia, D. Gunter, D. Skinner, G. Ceder, K. A. Persson, *APL Mater.* **2013**, *1*, 011002.
[87] A. L. Santhosha, N. Nazer, R. Koerver, S. Randau, F. H. Richter, D. A. Weber, J. Kulisch, T. Adermann, J. Janek, P. Adelhelm, *Adv. Energy Mater.* **2020**, *10*, 2002394.
[88] K. Okamoto, S. Kawai, *Jpn. J. Appl. Phys.* **1973**, *12*, 1130.
[89] B. Jache, B. Mogwitz, F. Klein, P. Adelhelm, *J. Power Sources* **2014**, *247*, 703.
[90] H. Grijalva, M. Inoue, S. Boggavarapu, P. Calvert, *J. Mater. Chem.* **1996**, *6*, 1157.
[91] K. Jiang, Z. Chen, X. Meng, *ChemElectroChem* **2019**, *6*, 2825.
[92] S. Terlicka, P. Darlak, N. Sobczak, J. J. Sobczak, *Materials* **2022**, *15*, 9024.